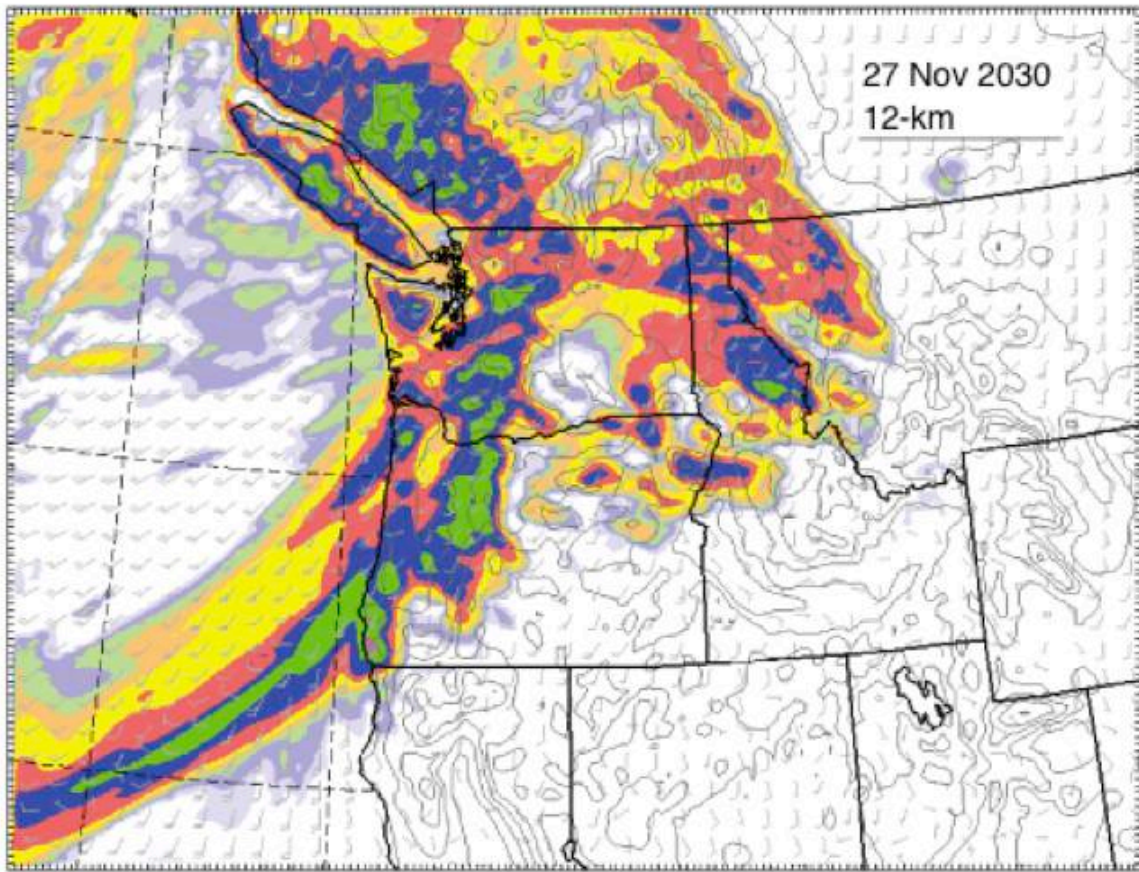


# Effect of Climate Change on the Hydrology of the Chehalis Basin



Future storm projected by the regional climate model used in this study (*Source: Eric Salathé*)

*Prepared by*

Guillaume Mauger, Se-Yeun Lee, Christina Bandaragoda,  
Yolande Serra, and Jason Won.

Climate Impacts Group, University of Washington

July 8, 2016



# Contents

---

<b>Background .....</b>	<b>4</b>
1.1 Climate Change in the Pacific Northwest .....	4
1.1.1 Greenhouse gas scenarios .....	4
1.1.2 Projected changes in temperature and precipitation .....	5
1.2 Climate change impacts on flooding.....	6
1.2.1 Sea Level Rise: .....	6
1.2.2 Snowpack:.....	6
1.2.3 Heavy Rains .....	6
1.2.4 Sediment .....	7
<b>Previous Flood Projections.....</b>	<b>8</b>
<b>Climate Data &amp; Models .....</b>	<b>9</b>
1.3 Observations .....	10
1.3.1 Weather Station Data .....	10
1.3.2 Gridded Observations .....	10
1.4 Projections.....	13
1.4.1 Statistically Downscaled Projections .....	13
1.4.2 Dynamically Downscaled Projections .....	14
1.5 WRF bias-correction .....	17
1.5.1 validating the WRF bias-correction: Historical .....	19
1.5.2 validating the WRF bias-correction: Future .....	20
<b>Hydrologic Data &amp; Modeling.....</b>	<b>21</b>
1.6 Observations .....	22
1.7 VIC Hydrologic Model .....	23
1.7.1 Overview .....	23
1.7.2 Configuration .....	23
1.7.3 Streamflow Routing.....	24
1.8 DHSVM Hydrologic model.....	25
1.8.1 Overview.....	26
1.8.2 Model Domain .....	26
1.8.3 Time step.....	27
1.8.4 Inputs.....	27
<b>Post-processing.....</b>	<b>32</b>
1.9 Model spin-up .....	32
1.10 Daily bias-correction.....	33
1.11 StreamFlow Statistics.....	34

---

1.11.1	Time periods .....	34
1.11.2	Extreme Flows .....	34
1.12	Data structure .....	35
1.12.1	Streamflow data .....	36
<b>Task 1 Results: Evaluating Changes in Rainfall.....</b>		<b>37</b>
1.13	WRF precipitation Projections.....	37
1.14	Assessing the drivers of Heavy precipitation.....	39
<b>Task 2 Results: Projected changes in streamflow .....</b>		<b>42</b>
<b>References.....</b>		<b>48</b>
<b>Appendix A: Links to Project Code, Models, and Data .....</b>		<b>53</b>

*Recommended citation format:* Mauger, G.S., S.-Y. Lee, C. Bandaragoda, Y. Serra, J.S. Won, 2016. Effect of Climate Change on the Hydrology of the Chehalis Basin. Report prepared for Anchor QEA, LLC. Climate Impacts Group, University of Washington, Seattle.

*Funding Source:* This project was funded by the Washington State Recreation and Conservation Office (RCO #15-1479) via a sub-contract with Anchor QEA, LLC.

---

## Background

---

Recent flooding in the Chehalis basin has led managers, residents, and others to begin evaluating options for managing flood risk in the future (e.g., Ruckleshaus Center 2012). Climate change is expected to both increase the risk of winter flooding and decrease summer low flows – with implications for human communities and ecosystems alike. This document summarizes the results of a study aimed at providing initial estimates of the impacts of climate change on streamflow in the Chehalis River basin. The specific objectives of this work were to:

1. Refine projections of changing hydrology in the Chehalis River Basin,
2. Supply the larger project team with new inputs for hydraulic and ecosystem models, and
3. Evaluate the potential for climate change to alter the proportion of runoff originating above the proposed dam during flood events.

### 1.1 Climate Change in the Pacific Northwest

#### 1.1.1 *Greenhouse gas scenarios*

Since it is impossible to predict the exact amount of greenhouse gas emissions resulting from future human activities, scientists use greenhouse gas scenarios to represent a range of different future conditions. These “what if” scenarios are used to drive global model simulations, which provide estimated changes in temperature, precipitation, and other aspects of the Earth’s climate.

Datasets used in this study include both the more recent greenhouse gas scenarios – dubbed Representative Concentration Pathways, or RCPs (Van Vuuren et al. 2011) – as well as the previous set, stemming from the Special Report on Emissions Scenarios, or SRES (Nakicenovic et al. 2000, for more information, see Chapter 1 of Mauger et al. 2015).

**Table 1.** Greenhouse gas scenarios used in this report.

<i>Greenhouse gas scenarios</i>	<i>Scenario characteristics</i>	<i>Description used in this report</i>
<i>RCP 4.5</i>	A low scenario in which greenhouse gas emissions stabilize by mid-century and fall sharply thereafter.	“Low”
<i>SRES A1B</i>	A medium scenario in which greenhouse gas emissions increase gradually until stabilizing in the final decades of the 21 <sup>st</sup> century.	“Moderate”
<i>RCP 8.5</i>	A high scenario in which greenhouse gas emissions continue to increase until the end of the 21 <sup>st</sup> century.	“High”

### 1.1.2 Projected changes in temperature and precipitation

The Puget Sound region is projected to warm rapidly during the 21<sup>st</sup> century (Figure 1). Prior to mid 21<sup>st</sup> century, the projected increase in air temperatures is about the same for all greenhouse gas scenarios, a result of the fact that a certain amount of warming is already “locked in” due to past emissions and existing infrastructure. After about 2050, projected warming depends on the amount of greenhouse gases emitted globally in the coming decades. For the 2050s (we use 30-year averages to represent the climate of the central decade, so the 2050s refers to the average over 2040-2069) annual average air temperature in Washington State is projected to rise +4.3°F to +5.8°F, on average, for a low (RCP 4.5) and a high (RCP 8.5) greenhouse gas scenario, respectively (Mote et al. 2013), relative to the 50-year period 1950-1999.

Natural variability has a large influence on regional precipitation, causing ongoing fluctuations between wet and dry years and between wet and dry decades. Climate models project only small changes in annual, fall, winter, and spring precipitation: instead, changes in seasonal precipitation will continue to be primarily driven by year-to-year variations rather than long-term trends. Models are more consistent in projecting a decline in summer precipitation for the region. As described below, changes in heavy rain events are projected to be much more pronounced than for annual and seasonal precipitation, and are likely to exceed the range of natural variability within this century (Trenberth 2011).

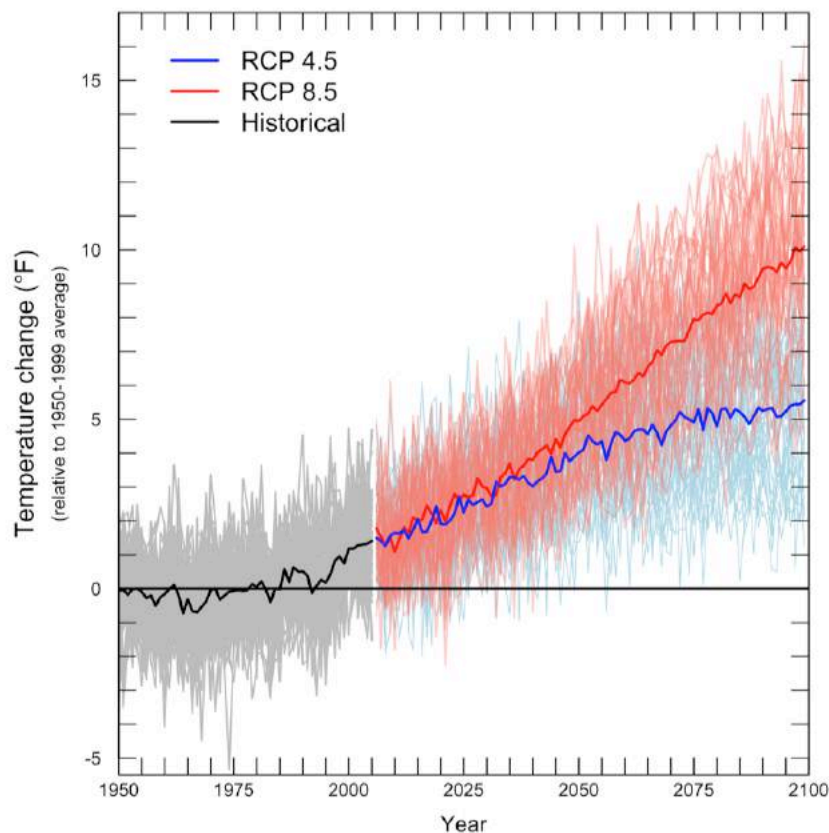


**Figure 1.** All scenarios project warming for the 21<sup>st</sup> century. The graph shows average yearly temperatures for the Pacific Northwest relative to the average for 1950-1999 (gray horizontal line). The black line shows the average simulated temperature for 1950–2011, while the grey lines show individual model results for the same time period. Thin colored lines show individual model projections for two emissions scenarios (low: RCP 4.5, and high: RCP 8.5 – see Section 3 for details), and thick colored lines show the average among models projections for each scenario (Data Source: Taylor et al. 2012).

## 1.2 Climate change impacts on flooding

In the Pacific Northwest, climate change is expected to impact flooding via the following four primary mechanisms.

### *1.2.1 Sea Level Rise:*

Higher sea level can increase the extent, depth, and duration of flooding by making it harder for flood waters in the rivers and streams to drain to the sea. Globally, sea level rose by about 7 inches from 1900-2000, and the most recent assessment of West Coast sea level rise (NRC 2012) projects an additional rise of 24 in. (range: 4 to 56 in.), on average for the Pacific Northwest, by the year 2100 (relative to 2000).

Sea level rise will affect flooding near the mouth of the Chehalis River, particularly near the towns of Aberdeen and Hoquiam, and may affect water quality by elevating groundwater levels and increasing the extent of saltwater intrusion. Increased inundation and erosion due to sea level rise could also cause habitat loss in low-lying areas, locations with highly erodible sediments, and areas where inland migration of coastal habitats is hindered by bluffs or human development. Changes in the salinity of estuarine waters may also affect plant and animal communities.

### *1.2.2 Snowpack:*

As air temperatures warm, snow is projected to accumulate less in winter and melt more rapidly in spring and summer. Due to its generally low elevation and proximity to the Pacific Ocean, the hydrology of the Chehalis basin can be classified as “rain dominant”: very little winter precipitation falls as snow. As a result, the basin exhibits a seasonal cycle in streamflow that closely matches the seasonal variations in precipitation. Nonetheless, about 23% of the basin area does experience a notable accumulation of snow each winter, and some of the highest elevation headwaters of the basin frequently retain snow into June and July.

Historically, monthly snow accumulation in the Chehalis basin has peaked on February 1<sup>st</sup>. By the 2050s (2040-2069), average February 1<sup>st</sup> snowpack in the basin is projected to decline by about 80%, relative to 1970-1999 (based on both a high and a low greenhouse gas scenario; Mote et al. 2015). Since snow retains water from fall and winter storms, this shift from snow to rain is projected to result in a direct increase in flood risk as precipitation from these storms contributes directly to runoff (Tohver et al. 2014).

### *1.2.3 Heavy Rains*

Given the warm winter temperatures that predominate in the Chehalis basin, heavy rain events are expected to be the primary driver of winter flood risk. In the Pacific Northwest, the majority of heavy rain events can be classified as Atmospheric River events (sometimes referred to as “pineapple express” events). Atmospheric Rivers (ARs) are characterized by a narrow band of

elevated humidity drawn from the tropics (or sub-tropics) to the mid-latitudes during winter storms. These can result in high rates of precipitation, particularly on the windward slopes of coastal and inland mountain ranges.

Most observational studies find increases in both the frequency and intensity of heavy precipitation in Western Washington (e.g., Mass et al. 2011, Rosenberg et al. 2010, Dulière et al. 2013). Similarly, current research is consistent in projecting an increase in the frequency and intensity of heavy rain events as the climate warms. For example, Warner et al. (2015) found that the top 1% daily rainfall events in Western Oregon and Washington will intensify by 22% (range: 5 to 34%) by the 2080s (2070-2099, relative to 1970-1999, for RCP 8.5). These high intensity events are also projected to occur more frequently: occurring about 7 days per year (range: 4 to 9 days per year) by the 2080s in comparison to 2 days per year historically.

#### *1.2.4 Sediment*

Winter rates of sediment transport, erosion, and landslides are all expected to increase as a result of climate change. Heavy rain events reduce slope stability by rapidly raising the water table (or groundwater elevation) and by enhancing water drainage through the soil to lower layers (Bogratti et al. 2010). In addition, intense rainfall can erode surface sediments, and higher streamflow during these events can erode stream banks and transport more sediment within the stream and along the stream bed (Curran et al. in review). These events can also lead to increased landslide risk: wetter soils are heavier, can absorb less precipitation (thus increasing runoff), and have greater lubrication among soil layers (Henn et al. 2015, Iverson et al. 2015).

Even as more sediment is transported downstream, sea level rise is expected to make it harder for the river to transport that sediment to the Pacific Ocean. Higher seas impose a backwater effect, reducing flow rates and increasing the rate of settling.

Sediment deposition in a river channel will result in reduced capacity and an increased risk of flooding. Given the likely increase in sediment mobilization and transport combined with a likely decrease in the ability of sediment to exit the system, climate change is likely to result in reduced channel capacity in the Chehalis river system, particularly in the lower reaches of the river.

## Previous Flood Projections

Several previous studies have quantified hydrologic changes in the Pacific Northwest, including changes in streamflow at specific sites within the Chehalis basin (e.g., Hamlet et al. 2013, Salathé et al. 2014), from which projected changes in flood risk can be derived. Initial efforts, comparing the results of these two studies, showed strong disagreement among estimates, ranging from small decreases in flood risk to a near doubling by mid-century (Figure 2). Unfortunately, these differences are strongly associated with differences in the approaches used to produce the estimates, in particular regarding the approaches used in developing the climate projections that serve as input to the hydrologic modeling. Other studies have since confirmed the strong dependence of modeling approach on projections of change (e.g., Mendoza et al. 2015). Along with the prospect of further refinements to the modeling and post-processing approaches, this sensitivity to the choice of methodology was a key motivation for the current study. In the sections below, we highlight where improvements have been made to previous approaches. The analysis also includes multiple datasets and models, intended to facilitate similar comparisons in the new dataset.

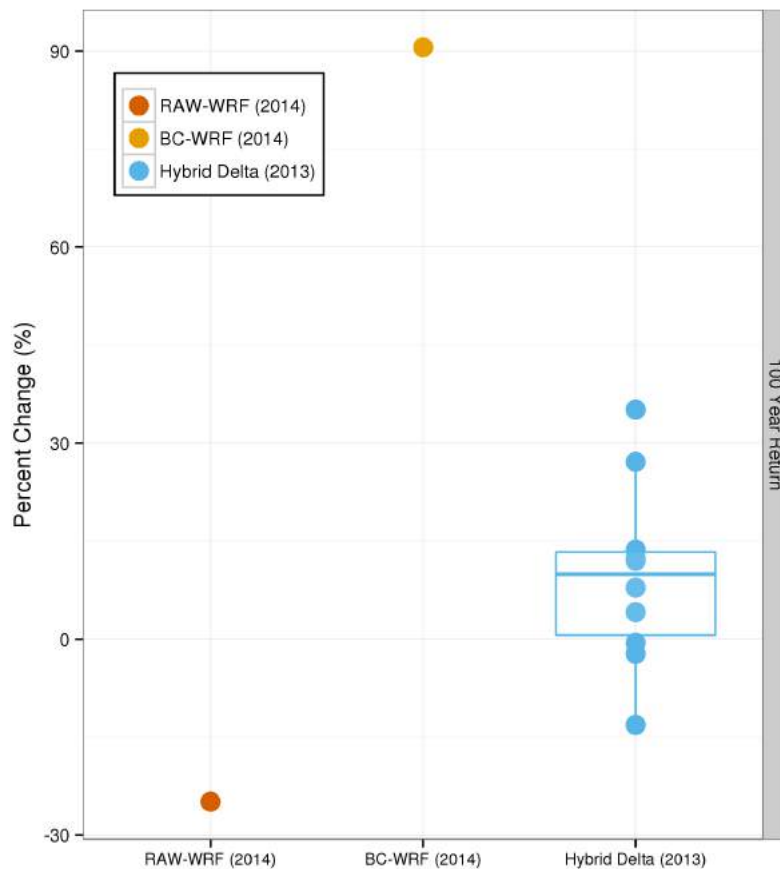


**Figure 2.** Large differences among previous estimates of the change in the 100-year flood volume (%) for the Chehalis River at Grand Mound. Projections are based on two different approaches to “downscaling” global climate model projections (see section below for a definition): (1) statistical (“Hybrid Delta”, Hamlet et al. 2013; change assessed for the 2040s, or 2030-2059) and (2) dynamical (“WRF”, Salathé et al. 2014; see Section 1.4.2). There are two different WRF projections: one based on the raw regional climate model simulations (“RAW-WRF”) and another based on the bias-corrected simulations (“BC-WRF”). All changes are assessed for a moderate greenhouse gas scenario (SRES A1B, see Table 1) for the 2050s (2040-2069) relative to 1970-1999.

## Climate Data & Models

This section describes the observed and projected future climate datasets that were used to both evaluate precipitation simulations and to drive hydrologic simulations of changing streamflow. With the exception of the point observations used for initial validation of the regional climate model simulations, all of the datasets used in this study provide gridded estimates of daily climate – either interpolated from observations or simulated – at a spatial resolution of 1/16-degree (about 5 km x 7 km, see Table 2).

**Table 2.** Gridded climate datasets used in this study

<i>Dataset</i>	<i>Model</i>	<i>Historical</i>	<i>Future</i>		
			<i>Low Emissions (RCP 4.5)</i>	<i>Moderate Emissions (SRES A1B)</i>	<i>High Emissions (RCP 8.5)</i>
bcLivneh <sup>*</sup>	N/A ( <i>based on obs.</i> )	1950-2013	--	--	--
bcMACA <sup>†</sup>	bcc-csm1-1-m	1950-2005	2006-2099	--	2006-2099
bcMACA	CanESM2	1950-2005	2006-2099	--	2006-2099
bcMACA	CCSM4	1950-2005	2006-2099	--	2006-2099
bcMACA	CNRM-CM5	1950-2005	2006-2099	--	2006-2099
bcMACA	CSIRO-Mk3-6-0	1950-2005	2006-2099	--	2006-2099
bcMACA	HadGEM2-CC365	1950-2005	2006-2099	--	2006-2099
bcMACA	HadGEM2-ES365	1950-2005	2006-2099	--	2006-2099
bcMACA	IPSL-CM5A-MR	1950-2005	2006-2099	--	2006-2099
bcMACA	MIROC5	1950-2005	2006-2099	--	2006-2099
bcMACA	NorESM1-M	1950-2005	2006-2099	--	2006-2099
rawWRF <sup>‡</sup>	CCSM3	1970-1999	--	2000-2069	--
rawWRF	ECHAM5	1970-1999	--	2000-2069	--
bcWRF <sup>§</sup>	CCSM3	1970-1999	--	2000-2069	--
bcWRF	ECHAM5	1970-1999	--	2000-2069	--

<sup>\*</sup> Bias-adjusted version of the observationally-based Livneh et al. 2013 gridded daily meteorological dataset. The dataset is adjusted to match the monthly time series from PRISM (Daly et al. 2004, 2008).

<sup>†</sup> Bias-adjusted version of the statistically downscaled Multivariate Adaptive Constructed Analogs (MACA, Abatzaglou and Brown 2011) gridded daily climate projections. The dataset is adjusted to match the 1950-2011 climatology from PRISM (Daly et al. 2004, 2008).

<sup>‡</sup> Weather Research and Forecasting (WRF) mesoscale climate model ([www.wrf-model.org](http://www.wrf-model.org), Skamarock et al. 2005). Simulations are based on the previous set of global climate model projections; newer simulations will be available in late 2016.

<sup>§</sup> Bias-adjusted version of the dynamically downscaled WRF projections. The dataset is bias-corrected using the observationally-based bcLivneh dataset listed above and described in the text.

## 1.3 Observations

### 1.3.1 *Weather Station Data*

Hourly precipitation observations from NOAA’s Cooperative Observer program (COOP, REFERENCE) were obtained from the National Center for Environmental Information (NCEI, Table 3). Hourly, 6-hourly and daily rainfall data sets are created by summing the mm per hour from the raw COOP data files over these time periods (for 6-h and 24-h rainfall) and adding in zeros as needed where no rainfall was recorded (the NOAA entries are left blank when there is no precipitation). If 33% of the data over the period (6-hours, 24-hours) are missing the period is assigned a missing value. These time-continuous hourly, 6-hourly and daily rainfall files are used to calculate the percentiles for each year and for the period as a whole along with all the times when the percentile rain threshold was equaled or exceeded. Although both 6-hourly and daily data were processed, analysis of model biases was performed only on the daily data. Extension to 6-hourly and 2-day precipitation could easily be undertaken in future work.

**Table 3.** Hourly weather station observations obtained for evaluating the regional climate model simulations. About six of the 14 stations are outside of the Chehalis basin – these were included based on both proximity and quality of the record. For comparison with the regional model simulations, data were only used for the years 1970-2010.

<i>Site ID</i>	<i>Name</i>	<i>Lat.</i>	<i>Long.</i>	<i>Elev. (ft)</i>	<i>Years</i>
450013	Aberdeen 20NNE	47.26	-123.71	435	01/01/1970—12/31/2010
451277	Centralia 1W	46.71	-122.98	190	01/01/1970—12/31/2010
451457	Cinebar 2 E	46.61	-122.50	1001	01/01/1970—12/31/2010
455549	Montesano 1 S	46.97	-123.61	25	09/01/1981—12/31/2010
456864	Quinault RS	47.47	-123.85	220	01/01/1970—12/31/2010
456896	Rainier Ohanapecosh	46.73	-121.57	1950	01/01/1970—12/31/2010
456909	Randle 1 E	46.53	-121.93	900	01/01/1970—12/31/2010
459112	Westport 2 S	46.87	-124.11	20	01/01/1970—07/28/2004
459485	Yelm	46.95	-122.60	350	01/01/1970—12/31/1978
451064	Camp Grisdale	47.37	-123.60	820	01/01/1970—09/19/1985
456114	Olympia Airport	46.97	-122.90	217	01/01/1970—12/31/2010
457294	Sam Henry Mountain	46.52	-123.02	1460	11/13/1980—02/23/1993
458788	Vanson Peak	46.42	-122.15	4931	11/04/1980—08/09/1985
459358	Winters Mountain	46.45	-122.32	3650	11/24/1980—09/16/2009

### 1.3.2 *Gridded Observations*

Surface weather observations – in particular long-term high-quality records – are typically sparse in spatial coverage, and tend to be biased towards low elevation areas near population centers. This means that point observations are generally sub-optimal for use in hydrologic modeling studies, in which the manifestation of large-scale weather patterns may be very different from one part of the watershed to another – in particular in areas with complex terrain. In addition, the

two hydrologic models used in this study employ a gridded approach, in which daily weather conditions must be developed for each input grid cell for use in estimating the water balance.

As a result, numerous approaches have been developed to produce spatially distributed and temporally complete estimates of daily temperature, precipitation, and winds for use in driving hydrologic model simulations (e.g., Maurer et al. 2002, Daly et al. 2002, Di Luzio et al. 2008, Hamlet and Lettenmaier 2005, Hamlet et al. 2013, Livneh et al. 2013, 2015). Although the methods vary, the general approach is to interpolate weather observations onto a grid and then apply corrections based on proximity and topographic similarity.

In this study we use data derived from the 1/16-degree Livneh v1.1 dataset (version 15Oct2014, Livneh et al. 2015, <http://www.colorado.edu/lab/livneh/data>) with North American Extent into Canada to obtain gridded daily estimates of minimum and maximum temperature, precipitation and wind speed from Jan 1, 1950 to Dec 31, 2013. Although the focus of this work is the Chehalis River Basin, we develop the dataset for the entire Pacific Northwest domain, as this is the standard approach and it requires minimal additional effort.

The data were produced using daily surface weather observations from the NOAA Cooperative Observer (COOP) network. Gridded daily temperature and precipitation data were produced by correcting for known biases and interpolated to the output 1/16-degree (about 5 km x 7 km) grid using the synergraphic mapping system (SYMAP) algorithm. Temperature at each grid cell was then adjusted for elevation differences using a constant 6.5 °C/km lapse rate. Instead of using a fixed lapse rate, gridded precipitation values were scaled to match the long-term monthly mean from the Parameter-Elevation Regressions on Independent Slopes (PRISM) model

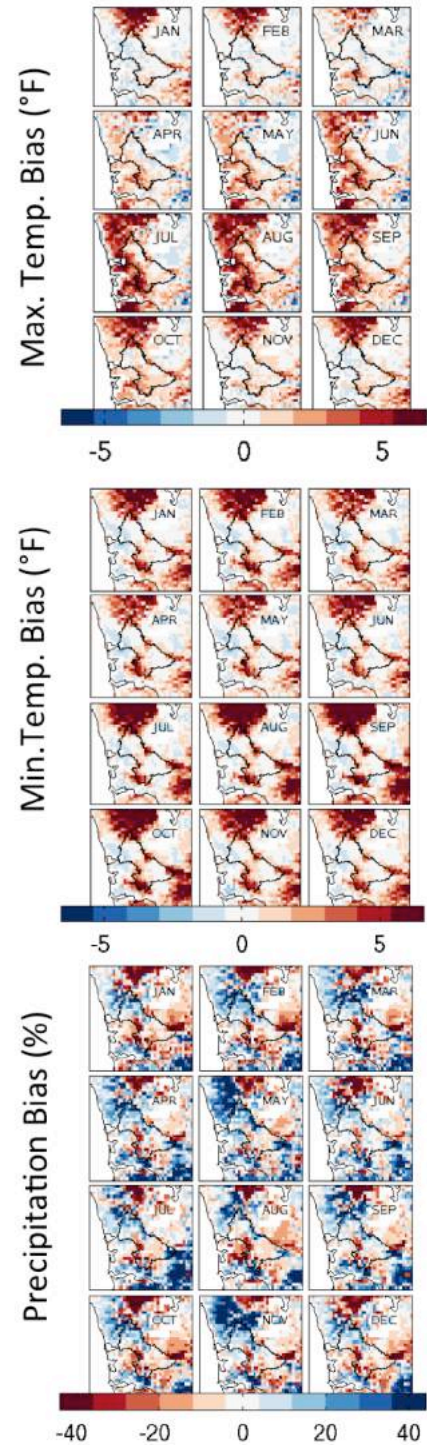


**Figure 3.** Differences in the monthly values of maximum temperature (top, °F), minimum temperature (middle, °F), and precipitation (bottom, %) for the Livnehv1.0/v1.1 dataset relative to the PRISM dataset (1950-2013).

(Daly et al. 2002, 2008). Wind data were not produced directly from observations, but from a reanalysis<sup>1</sup> of observations. Specifically, the NCEP-NCAR reanalysis wind data (Kalnay et al. 1996) was bi-linearly interpolated to the 1/16-deg Livneh grid.

Recent evaluations of the Livneh et al. (2013) dataset have shown that the fixed lapse rate assumption for temperature can result in substantial biases, since most observations are at low elevation and the atmosphere can deviate significantly from this rate of temperature change with altitude. In particular, temperatures at elevation can exhibit a substantial cold bias in the winter months. Figure 3 shows the biases between the monthly PRISM dataset (AN81M monthly, Daly et al. 2008) and the Livnehv1.0/v1.1 datasets for minimum/maximum temperature and precipitation. Temperature biases were largest in the mountains, where the Livneh dataset assumes a constant lapse rate for temperature. This has implications for hydrologic model simulations, since many elements of the water balance – snow accumulation and melt, evaporation, transpiration – depend non-linearly on the temperature. Sensitivity tests indicate that this can result in biased estimates in both historical conditions as well as the response to warming.

As a result of the temperature bias, in this study we have corrected the gridded Livneh meteorological dataset using monthly data from PRISM. Since the Livneh dataset extends into Canada, a PRISM climatology developed for British Columbia (PCIC, 2014) was applied to the Canadian portion of the domain. To do this, the monthly PRISM data was aggregated from its 1/24-degree native resolution to the 1/16-degree Livneh grid. Similarly, the PRISM climatology from PCIC was aggregated from 1/120-degree to 1/16-degree resolution. Whereas the climatology was used in the Canadian portion of the domain, the PRISM monthly time series from Jan 1950 – Dec 2013 was used for the U.S. portion of the domain.

Using the reference PRISM datasets, a simple bias adjustment was performed by adjusting the daily Livneh temperatures with the difference between the monthly Livneh dataset and the interpolated monthly PRISM temperature variables. For precipitation, a ratio was used in lieu of a difference. The final result was that the Livneh dataset has the same monthly climatology as the PRISM dataset. One additional correction was applied due to a complication in the method that arose for precipitation: when the monthly total in the Livneh dataset was zero but non-zero in the PRISM dataset, the consequence was an infinite ratio (divide by zero) for scaling the Livneh dataset. To avoid this, the daily precipitation data was simply scaled uniformly to match the PRISM monthly value instead of using a ratio.

---

<sup>1</sup> The term “Reanalysis” refers to models that are used to optimally combine a vast amount of surface, airborne, and satellite observations using a Bayesian framework, in order to obtain best estimates of evolving weather and climate patterns over the observational record.

The final resulting bias corrected training dataset (“bcLivneh”) covers an area between 41 – 53 N and 125 to 108W for Jan 1, 1950 to Dec 31, 2013.

## 1.4 Projections

Evaluating climate change impacts requires developing spatially relevant scenarios of projected changes in climate. Yet global climate models (GCMs) are typically available at much coarser scales (e.g., 100 km resolution). In these cases, “downscaling” can be used to relate the large-scale changes projected by GCMs to smaller-scale changes of relevance to impacts assessment. There are two general categories of downscaling approaches (for more on the two techniques, see WHCWG 2013):

1. **Statistical Downscaling**, in which projections are disaggregated using empirical relationships between GCM variations and observed weather characteristics, and
2. **Dynamical downscaling**, in which a regional climate model (RCM) simulation provides a physically-based estimate of local climate variations, using GCM outputs as a boundary condition.

For this study, we used projections employing both techniques, in order to provide a check on the results stemming from each approach.

### 1.4.1 *Statistically Downscaled Projections*

The statistically downscaled projections were obtained from the MACAv2-LIVNEH dataset (Multivariate Adaptive Constructed Analogues, Hegewisch and Abatzoglou 2016, Abatzoglou and Brown 2012). As with all statistical downscaling approaches, MACA was applied by using an observationally-based dataset to develop empirical relationships between coarse-scale global model projections and local-scale weather and climate variations. In this case the dataset used was Livneh v1.0 (on the US side) and Livneh v1.1 on the Canadian side (Livneh et al. 2013). MACA was applied at the daily time step, and used a multivariate constructed analogues approach, meaning that a historical library of observations was used to relate similar meteorological states in both the GCM and the observations.

Projections were based on 10 global models from the CMIP5 (Coupled Model Intercomparison Project Phase 5, Taylor et al. 2012) experiment. The 10 GCMs were selected from the larger set of CMIP5 simulations based on their ability to accurately represent the climate of the Pacific Northwest (Rupp et al. 2013, Table 1). The MACA downscaling was applied to the historical experiment (1950-2005) and two future projection experiments (2006-2099) for each GCM (i.e., 2 time series per GCM). The two projections were taken from a low (RCP 4.5) and a high (RCP 8.5) greenhouse gas scenario (Van Vuuren et al. 2011).

For consistency with the corrected Livneh et al. (2013) dataset used for this project, the MACA data were also bias-adjusted so that monthly MACA data matched PRISM. Corrections to the MACA dataset were computed by applying the difference between the average monthly values for temperature from the Livneh NAmerExt dataset (1950-2013) and the Livneh v1.0/v1.1 combination dataset (1950-2011). For precipitation, the ratio was used instead of the difference. These monthly corrections were applied to all daily values in each month of the MACAv2-LIVNEH dataset to correct both the historical and future values in the dataset.

#### 1.4.2 Dynamically Downscaled Projections

The dynamically downscaled projections were based on Regional Climate Model (RCM) simulations performed using the Weather Research and Forecasting (WRF) Mesoscale Model (<http://www.wrf-model.org>; Skamarock et al. 2005). The WRF model was implemented employing the approach described in previous work (Salathé et al. 2010, 2014). In this configuration, nested 36- and 12-km grids were used to downscale from the global atmospheric fields with grid spacings of approximately 100-200 km. The inner 12-km domain spans the region from northern California to southern British Columbia and from the coastal ocean to the Rocky Mountains (Figure 4). Although somewhat coarse in resolution for the domain of the Chehalis basin, the WRF model grid is sufficient to capture the general features of the watershed, including the area upstream of the proposed dam (Figure 5).

The WRF projections include an observationally-based historical simulation and 3 GCM projections. The observationally-based simulation was driven by the NCEP-NCAR Reanalysis Project (NNRP, Kalnay et al. 1996), which spans the years 1950-2010. The three other WRF simulations were based on global model projections (CCSM3 and

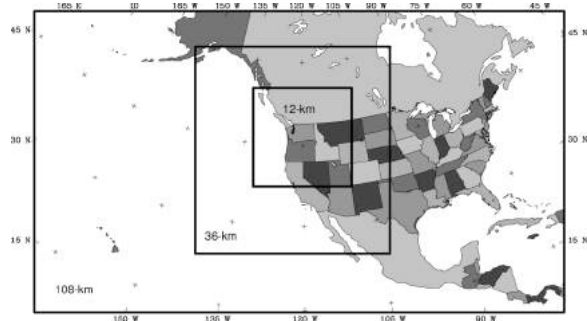


**Figure 4.** Domains for the WRF (Weather Research and Forecasting) regional model: Western US at 36-km and Pacific Northwest at 12-km resolution.

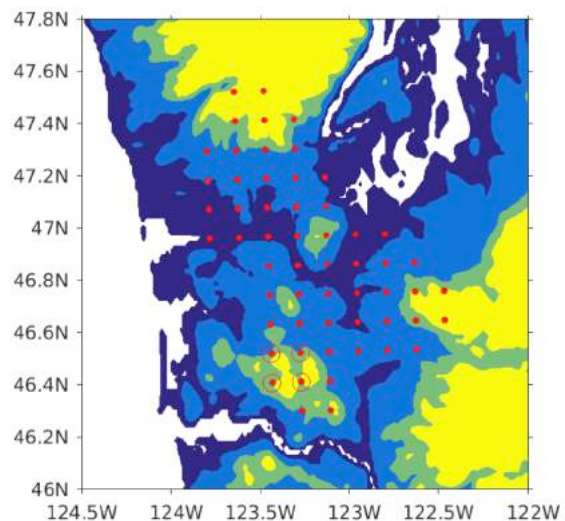


**Figure 5.** WRF 12 km grid points (red dots) that overlap with the Chehalis River basin. The four grid cells that overlap with the area upstream of the proposed dam are circled in red. The background shading shows the topography of the region, with the 330, 980, and 1640 ft (100, 300, and 500 m) contours.

ECHAM5) included in the CMIP3 (Coupled Model Intercomparison Project Phase 3, Meehl et al. 2007) experiment, in addition to one simulation based on the CCSM4 projections used in CMIP5 (Taylor et al. 2012). The CCSM4 run was only used in the precipitation analysis, and was excluded from the hydrologic simulations due to data limitations. For the WRF simulations, the historical time period (in which observed greenhouse gases are used to drive model simulation) spans from 1970-1999, while the future projections span from 2000-2069 and are based on moderate (SRES A1B) greenhouse gas scenario. In the case of CCSM4, the historical and future simulations span from 1950-2005 and 2006-2099, respectively, based on a low (RCP 4.5) greenhouse gas scenario.

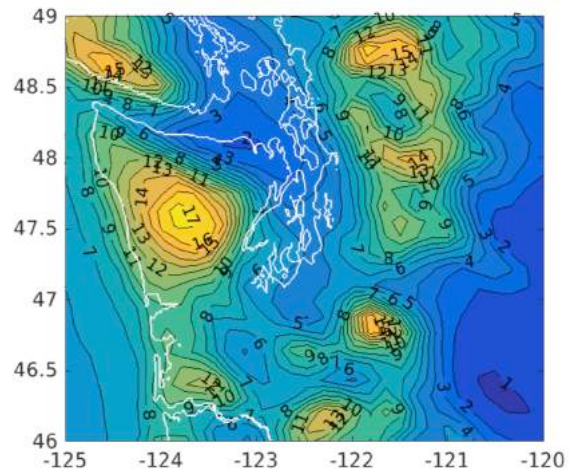


**Figure 6.** Average Oct-Nov precipitation (cm/month, for 1970-2010), based on the WRF NNRP simulation.

#### 1.4.2.1 Evaluating WRF precipitation

In order to determine model biases in precipitation for the historical period and any changes to precipitation frequency and intensity in the future period we examined four different precipitation thresholds: the 80<sup>th</sup>, 90<sup>th</sup>, 95<sup>th</sup> and 98<sup>th</sup> percentiles. WRF model data are provided at 6-hourly intervals, with precipitation being accumulated from the start of the model simulation. Thus, precipitation rate is calculated as the difference between model time steps. Time steps for which a previous time was not available from WRF, either because it is the first time in the simulation or because it is the first time after a restart has occurred, are set to a missing value. For the daily analyses model daily rainfall on day 1 is calculated as the difference between accumulated rainfall on day 1 at 06 UTC from that on day 0 at 06 UTC (except for CCSM4 which is the accumulation from 00 UTC on day 0 to day 1, i.e. the past 24 hours). The 6-hourly rainfall is the accumulated rainfall over the past 6 hours. Percentiles are based on rain rates above 0.1” (2.54 mm) in a time period (6 hours or 1 day). This threshold is chosen to roughly correspond with the lower limit of detectability of rain per hour for the in situ rain gauges. WRF has no definable limit to which rain is or is not present beyond selecting any value above 0, which may include unrealistically low values for precipitation.

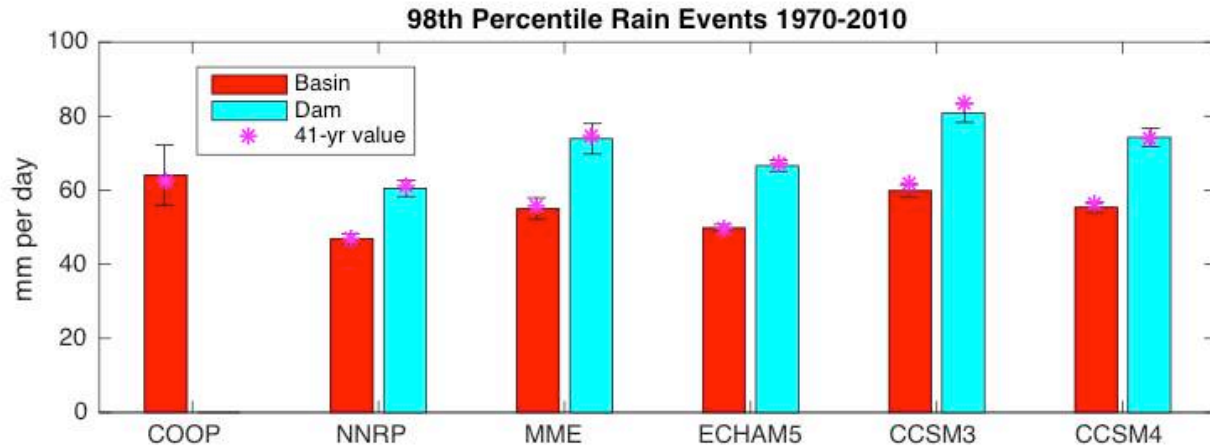


**Figure 7.** Comparison between observed precipitation extremes (COOP, average among all stations listed in Table 3) and those simulated by WRF. Results are shown for the 98<sup>th</sup> percentile in daily rainfall for the years 1970-2010, for both the entire basin (“Basin”, in red) and for just the area above the proposed dam (“Dam”, in blue). The average of the three global model projections is also shown, labeled MME (Multi-Model Ensemble). Error bars show the standard deviation for all years.

Maps of composite rainfall show that the basic features of precipitation in the region are captured by the WRF model (Figure 6). Extreme precipitation appears to also be well represented by the model. Figure 7 shows the average 98<sup>th</sup> percentile event in both the observations and the model. The comparison shows general agreement, and that the model does capture the higher precipitation totals in the area above the proposed dam.

Nonetheless, the analysis might be improved by using a higher resolution WRF grid to more accurately represent the topography (smoothed topography may lead to mis-representations of precipitation) and better distinguish between rain falling within the basin as opposed to outside of the watershed boundary (e.g., lee vs. windward side of the Willapa Hills – a key question given this area’s location upstream of the proposed dam).

#### 1.4.2.2 *Integrated vapor transport and precipitable water*

Previous research suggests that the primary factors affecting the magnitude of extreme precipitation events in the region are thermodynamic (Warner et al. 2015). In other words, the atmospheric dynamics are already optimized during atmospheric river events to maximize precipitation in the region, and are only limited by the concentration of water vapor available (due to moisture convergence) during a particular storm. In order to evaluate potential variations in moisture convergence we calculate composites of the daily mean total precipitable water vapor (TPW, column-integrated water vapor) and integrated vapor transport (IVT) for each precipitation threshold identified based on the percentiles listed above. These composites can be compared to understand the large-scale features associated with the rainfall above each threshold.

### 1.4.2.3 Principle components analysis

Principal components analyses (often referred to as Empirical Orthogonal Functions, or EOFs) were explored to identify the primary modes of IVT spatial variability associated with heavy precipitation events over the basin. Both a combined EOF and a complex EOF analysis were performed on the global model daily IVT fields. A combined EOF identifies the primary modes of variability in IVT associated with maximum variance in the combined zonal (East-West) and meridional (North-South) components of the vapor transport resulting in separate spatial patterns for the IVT components (the EOFs) based on their in-phase maximum variance. A complex EOF is similar to a combined EOF, but the maximum variance in the zonal and meridional winds associated with the primary modes of variability are not necessarily in-phase with one another. Because the complex EOF approach maximizes the variance in the transport components regardless of their phase, it is potentially a better approach for exploring the impact of any change to the path of AR events impinging on the basin in the future related to changes in the mean location of the mid-latitude storm track.

We performed an EOF analysis on daily IVT data for only those days when the daily precipitation was at or above the 90<sup>th</sup> percentile for that grid point. The 90<sup>th</sup> percentile was chosen as a compromise between increased sample size and the need to focus on high intensity rain events. Prior to calculating the combined EOF the two integrated transport terms, IQU and IQV, are centered (mean removed) and normalized (divided by the standard deviation). The anomalies are then weighted by the square root of the cosine of the latitude to account for the changing area of the model grid with latitude. The complex EOF is based on performing a single value decomposition of the complex matrix  $Z = IQU' + i*IQV'$ , where IQU' and IQV' are normalized anomalies, as defined as above. The real part of the complex EOFs are the spatial patterns associated with the zonal vapor transport, while the imaginary part of the complex EOFs are the spatial patterns associated with the meridional vapor transport. Similarly, the real part of the complex PCs represents the time variability of the modes for the zonal vapor transport, while the imaginary part of the complex PCs represents the time variability for the meridional vapor transport.

## 1.5 WRF bias-correction

The WRF outputs are on a curvilinear 12-km grid that is incompatible with the hydrological model. These were first spatially disaggregated (SD), via bi-linear interpolation, to rectangular coordinates on the 1/16-degree Livneh dataset grid. Two versions of the 1/16-degree WRF data were then produced:

1. “rawWRF”, in which the interpolated WRF data were used directly as input to hydrologic modeling, and

2. “bcWRF”, in which the interpolated WRF data were first bias-corrected to match the bcLivneh dataset.

The bias-correction process was applied to the raw WRF outputs utilizing the spatial disaggregation bias correction (SDBC, Liang et al, 1994) method. In this method, first the trend in the interpolated “SD” data (calculated as a 21-day, 31-year moving average) was removed from both the historical and future data. Second, the data were bias corrected to the Livneh training dataset utilizing the quantile mapping method (Li et al, 2010, Pierce et al, 2015). In this quantile mapping method, the distribution of 45-day periods of the historical RCM data was mapped to the same 45-day periods of data from the observed distribution from the Livneh training dataset. The differences (ratios) of the future RCM to the historical RCM at each quantile in the cumulative distribution function (CDF) were preserved in the final downscaled data to allow future distributions of the variables to change from that observed in the past. Such quantile mapping is known to alter the final trends in precipitation data, so as a final process we adjusted the mean precipitation to match that from observations (i.e. the presRat method from Pierce et al, 2015). Only the interior 15-days of the 45-days in the quantile mapping were saved to the final downscaled data in order to smooth results between 45-day periods of the year. Third, the trends were replaced upon the data. Finally, one last bias correction was performed on the historical data by adjusting the annual means of temperature and precipitation with respect to those from the Livneh training dataset.

For temperature, a quality control measure was taken to ensure that for each day the minimum temperature was less than or equal to the

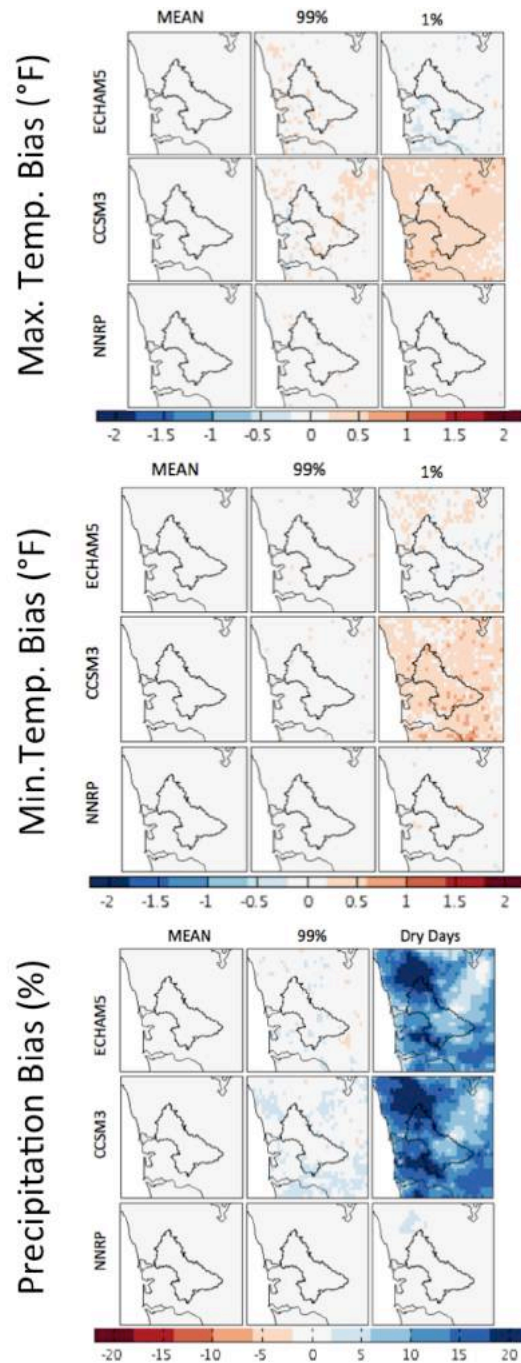


**Figure 8.** Differences between the historical bias-corrected WRF simulations and the bcLivneh dataset used for bias correction. Maps show the maximum temperature (top), minimum temperature (middle), and precipitation (bottom) for the mean (left), 99<sup>th</sup> percentile (middle) and 1<sup>st</sup> percentile / percentage of dry days (right). All numbers are sampled from the full daily record of each dataset.

maximum temperature. In cases where this was not true the minimum temperature for the day was set equal to the maximum temperature.

1.5.1 *validating the WRF bias-correction:*  
*Historical*

The downscaling process includes bias correction of the historical RCM temperature and precipitation simulations, which were adjusted to match the observationally-based training dataset (in this case, bcLivneh). The bias correction process was applied using fixed 45-day sub-periods in each year. By construction, comparisons of the distribution of the 15-days of saved bias-corrected RCM data to the corresponding 15-days of the training Livneh dataset show that the two agree almost exactly. However, comparisons over longer sub-periods likely exhibit some biases. To investigate such biases, we considered the distribution of temperature and precipitation over all days and all years of available data, and compared the 1<sup>st</sup> and 99<sup>th</sup> percentiles as well as the mean of the distribution to the observations. For precipitation, the percentage of dry days (precipitation < 0.01”) was used instead of the 1<sup>st</sup> percentile.

Figure 8 shows the historical biases, relative to the bcLivneh training dataset, that remain after bias correction. The biases are much lower for the bias-corrected reanalysis NNRP dataset than for the free-running climate model simulations, presumably because the reanalysis dataset started out much closer to the observations than the other simulations. Second, biases in temperature for the average and 99th percentile are very low across the region for all bcRCMs, but at the 1<sup>st</sup> percentile are approximately ±0.4°F scattered across the region. Third, there is a dry bias of about 2% in average precipitation values in parts of the interior Northwest, and some structure in the bias in the 99<sup>th</sup> percentile values. These may be related to the choice of a dry day threshold, which affects the bias-correction.

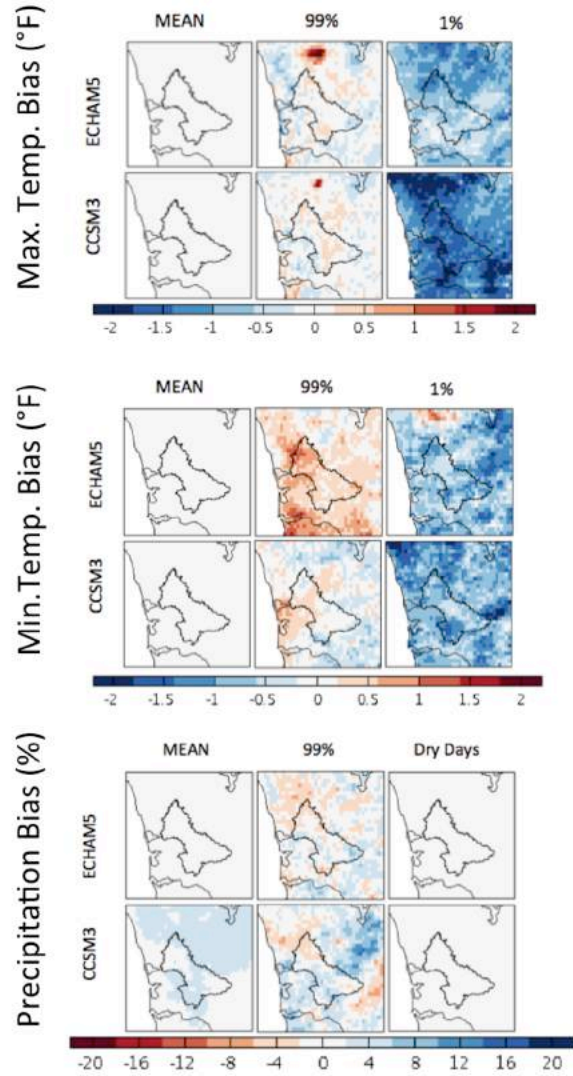


**Figure 9.** Differences between the changes projected by the bias-corrected and raw WRF datasets for the 2050s (2040-2069) relative to 1970-1999. Results are shown for the change in annual average maximum temperature (top, °F), minimum temperature (middle, °F), and precipitation (bottom, %) for the mean (left), 99<sup>th</sup> percentile (middle) and 1<sup>st</sup> percentile / percentage of dry days (right).

1.5.2 *validating the WRF bias-correction:*  
*Future*

The downscaling process aims to preserve the signal of climate change projected by the RCM with respect to the historical period. To assess potential biases introduced in this signal, we compare the changes in bcWRF and rawWRF for the 2050s (2040-2069) relative to the historical period (1971-1999). As above, by construction the signal of change over 15-day sub-periods in each year yields a nearly exact match when comparing to the bias-corrected to raw model projections. However, comparisons over longer sub-periods showed significant biases in the future projections, especially for the extremes.

Figure 9 shows the biases (difference between the projected changes in bcWRF and rawWRF) for the 1<sup>st</sup> percentile / percent dry days, 99<sup>th</sup> percentile, and average values in temperature and precipitation. Note that future projections in precipitation were calculated as a percent change, so the precipitation maps (bottom panel in Figure 9) show the differences in these percent changes. In general, there are essentially no differences in the average change projected for the 2050s for all variables. Although there are fairly substantial differences in the temperature extremes, the biases are much smaller in the vicinity of the Chehalis basin, and they are nearly non-existent for precipitation extremes.

Changes in flood risk in the Chehalis are primarily driven by extreme precipitation events, which typically involve rainfall accumulations that are substantially in excess of the annual 99<sup>th</sup> percentile (i.e. N-year precipitation events, defined as the annual daily maximum with a 1/N-% chance of exceedance). In order to evaluate the quality of the bias-correction for rare events such as these, we consider the 10-year precipitation event, which would roughly correspond to the 99.99<sup>th</sup> percentile event when considering the full daily record of precipitation. Figure 10 shows the bias in the change projected for the 10-year precipitation event from bcWRF compared to the rawWRF data. However, the 10-year event might under-sample extremes since there is a chance that the largest events might cluster in particular years. For comparison, we also include an alternative extreme precipitation measure, which may be more closely aligned with the bias correction approach: the 99.9<sup>th</sup> percentile of daily precipitation, sampled from a single distribution constructed from the full daily record of precipitation (approximately equivalent to the 3-year event).

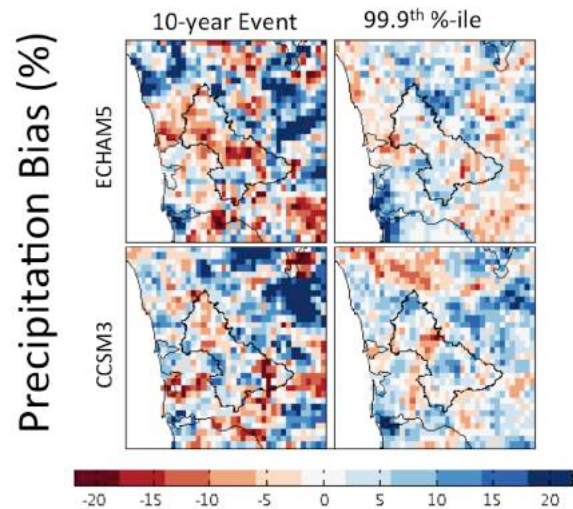


**Figure 10.** Same as Figure 8, except for precipitation extremes: showing the difference in the projected change in the 10-year precipitation event (left), and the 99.9<sup>th</sup> percentile in daily precipitation (right).

Figure 10 shows that projected changes in either extreme precipitation metric has both positive and negative biases spatially over the region with no indication of a systematic bias relating to geography, metric, or global model projection. In order to evaluate options for minimizing these differences, we performed sensitivity tests by varying the precise details of the bias correction procedure. No test resulted in a perfect match between the rawWRF and bcWRF extremes projections. However, one critical source of disagreement was corrected: testing indicates that there is a mismatch between the seasonal timing of heavy rain events in the Livneh observations and in the WRF simulations. As a result, the quantile mapping step in the bias correction was occasionally mapping relatively less extreme events in the WRF projections to much more extreme events in the observations, thereby exaggerating their magnitude. When the opposite occurred, the bias in the 10-year and 99.9% events remained unaffected since these were smaller events. This prompted us to expand the window used in quantile mapping from a width of 15 to 45 days.

Ultimately, a bias correction approach that is designed to correct the full probability distribution will likely always yield a mismatch when comparing extreme values in the simulated and observed datasets. We attribute the remaining biases to two principal factors: (1) the fact that the extremes are by definition poorly sampled and therefore difficult to bias correct robustly, and (2) differences in the timing of extreme events that are not captured by a 45-day window.

## Hydrologic Data & Modeling

---

This study uses observed streamflow from USGS observations and simulated streamflow from two hydrologic models: the Variable Infiltration Capacity (VIC) macroscale hydrologic model and the Distributed Hydrologic Soil Vegetation Model (DHSVM). Historical and future streamflow estimates were produced at sites in or near the Chehalis River basin, selected in consultation with project partners (Table 4).

Due to limited time and budget, *neither hydrologic model was calibrated*. Future work could further refine these results by calibrating one or both models for the Chehalis basin.

**Table 4.** Streamflow sites selected for output from hydrologic model simulations. The table lists the hydrologic model used to develop streamflow estimates at each site (not all sites were simulated by both hydrologic models), and the water years (Oct-Sep) of quality-controlled observations. Sites listed in bold were bias corrected – in all 11 sites had the minimum required 30 water years of valid data.

<i>ID</i>	<i>Site Name</i>	<i>Lat.</i>	<i>Long.</i>	<i>Model</i>	<i>Water Yrs.</i>
12019310	Chehalis River above Mahaffey Creek near Pe Ell	46.54532	-123.29872	BOTH	2014-2015
<b>12020000</b>	<b>Chehalis River near Doty, WA</b>	<b>46.61750</b>	<b>-123.27639</b>	<b>BOTH</b>	<b>1951-2015</b>
12020500	Elk Creek near Doty, WA	46.62833	-123.33056	DHSVM	1968-1970
12020525	Elk Creek below Deer Creek near Doty	46.63472	-123.29556	BOTH	2011-2011
12020800	SF Chehalis River near Wildwood	46.44500	-123.08250	BOTH	n/a
12020900	South Fork Chehalis River near Boistfort, WA	46.52722	-123.11611	DHSVM	1966-1980

<i>ID</i>	<i>Site Name</i>	<i>Lat.</i>	<i>Long.</i>	<i>Model</i>	<i>Water Yrs.</i>
12021000	SF Chehalis River at Boistfort	46.54583	-123.13194	BOTH	1962-1965
12021800	Chehalis River near Adna, WA	46.62583	-123.10056	DHSVM	n/a
12023500	Chehalis River near Chehalis, WA	46.64167	-123.01528	DHSVM	n/a
12024000	SF Newaukum River near Onalaska, WA	46.57583	-122.68389	BOTH	1958-1971
12024400	NF Newaukum River above Bear Creek near Forest	46.66750	-122.76889	BOTH	n/a
12024500	North Fork Newaukum River near Forest, WA	46.65556	-122.77778	DHSVM	1961-1966
<b>12025000</b>	<b>Newaukum R near Chehalis</b>	<b>46.62028</b>	<b>-122.94389</b>	<b>BOTH</b>	<b>1951-2015</b>
12025100	Chehalis River at WWTP at Chehalis, WA	46.66111	-122.98278	DHSVM	n/a
12025310	Salzer Creek at Centralia	46.69972	-122.92806	DHSVM	2011-2011
<b>12025700</b>	<b>Skookumchuck River near Vail, WA</b>	<b>46.77278</b>	<b>-122.59278</b>	<b>BOTH</b>	<b>1968-2015</b>
<b>12026150</b>	<b>Skookumchuck R. blw. Baldy Run Crk. nr. Centralia</b>	<b>46.79028</b>	<b>-122.73417</b>	<b>BOTH</b>	<b>1970-2015</b>
<b>12026400</b>	<b>Skookumchuck River near Bucoda, WA</b>	<b>46.78889</b>	<b>-122.92306</b>	<b>BOTH</b>	<b>1969-2015</b>
12026590	Hanaford Creek at Mouth	46.74750	-122.93556	DHSVM	n/a
12027000	Lincoln Creek at Mouth	46.73611	-123.17778	BOTH	n/a
<b>12027500</b>	<b>Chehalis River near Grand Mound, WA</b>	<b>46.77611</b>	<b>-123.03444</b>	<b>BOTH</b>	<b>1951-2015</b>
12029000	Black River at Little Rock, WA	46.90278	-123.02222	DHSVM	n/a
12030000	Rock Creek at Cedarville, WA	46.86806	-123.30694	BOTH	1951-1971
<b>12031000</b>	<b>Chehalis River at Porter, WA</b>	<b>46.93944</b>	<b>-123.31306</b>	<b>BOTH</b>	<b>1953-2015</b>
12032500	Cloquallum Creek at Mouth	47.00472	-123.38639	BOTH	1951-1972
12033000	Chehalis River at South Elma, WA	46.98222	-123.41111	DHSVM	1951-1951
12033500	East Fork Satsop River near Matlock, WA	47.16250	-123.36667	DHSVM	n/a
12034000	Bingham Creek near Matlock, WA	47.16111	-123.39583	DHSVM	n/a
12034200	East Fork Satsop River near Elma, WA	47.12778	-123.41667	DHSVM	1958-1971
<b>12035000</b>	<b>Satsop River near Satsop, WA</b>	<b>47.00083</b>	<b>-123.49361</b>	<b>BOTH</b>	<b>1951-2015</b>
12035002	Chehalis River near Satsop, WA	46.97222	-123.49028	DHSVM	2003-2008
<b>12035400</b>	<b>Wynoochee River near Grisdale</b>	<b>47.38056</b>	<b>-123.60861</b>	<b>BOTH</b>	<b>1966</b>
<b>12036000</b>	<b>Wynoochee River above Save Creek</b>	<b>47.29917</b>	<b>-123.65194</b>	<b>BOTH</b>	<b>1951-2015</b>
12036400	Schafer Creek near Grisdale, WA	47.20444	-123.61389	DHSVM	1987-1996
12036500	Wynoochee River near Montesano, WA	47.17967	-123.62500	DHSVM	n/a
12036650	Anderson Creek near Montesano, WA	47.12389	-123.65472	DHSVM	1973-1985
<b>12037400</b>	<b>Wynoochee River above Black Creek nr. Montesano</b>	<b>47.01167</b>	<b>-123.65417</b>	<b>BOTH</b>	<b>1957-2015</b>
12039005	Humtulpis River at Highway 101	47.23167	-123.97278	VIC	2003-2015
n/a	Black River near SR 12	46.83008	-123.18549	BOTH	n/a
n/a	Stillman Creek at Mouth	46.55351	-123.13856	BOTH	n/a
n/a	Independence Creek at mouth	46.79808	-123.16552	BOTH	n/a
n/a	Wishkah River at Mouth	46.97418	-123.80908	VIC	n/a
n/a	Hoquiam River at Mouth	46.97088	-123.87724	VIC	n/a
n/a	Humtulpis River at Mouth	47.04528	-124.04934	VIC	n/a
n/a	Darlin Creek Fish Passage Project	46.95777	-123.03890	DHSVM	n/a
n/a	Wisner Creek Bunker Road	46.65932	-123.04941	DHSVM	n/a
n/a	Bunker Road and Wisner Creek Projects (2)	46.68186	-123.23753	DHSVM	n/a
n/a	Great Eight Barrier Removal Project (8)	46.76046	-123.19220	DHSVM	n/a
n/a	Harstad Crk Mdl Satsop Rd Fish Barrier Correction Proj.	47.06285	-123.50125	DHSVM	n/a
n/a	Boyer Road Fish Barrier Correction Project	46.94624	-123.29400	DHSVM	n/a
n/a	Eaton Creek South Bank Road Fish Barrier Corr. Proj.	46.94372	-123.35173	DHSVM	n/a
n/a	Taylor Crk Taylors Ferry Rd Fish Barrier Corr. Proj.	46.97396	-123.38910	DHSVM	n/a
n/a	Mox Chehalis Branch Rd Fish Barrier Correction Proj.	47.04322	-123.24942	DHSVM	n/a
n/a	Unnamed Trib. to Stearns Crk Fish Barrier Removal	46.56158	-122.96461	DHSVM	n/a
n/a	Prairie Creek Fish Barrier Removal	46.67017	-123.14830	DHSVM	n/a
n/a	Van Ornum Creek Fish Barrier Removal	46.65451	-123.09674	DHSVM	n/a
n/a	Gaddis Creek near South Band Road Fish Barrier	46.93147	-123.32708	DHSVM	n/a
n/a	Carlisle Lake	46.57038	-122.73679	DHSVM	n/a
n/a	Chehalis River DHSVM Model outlet	46.96998	-123.81667	DHSVM	n/a

## 1.6 Observations

Daily streamflow observations were obtained for all USGS stations with at least 30 complete water years of valid data (Table 4, <http://waterdata.usgs.gov/nwis>). These were assessed for quality control issues and missing data, and for the influence of major alterations in flow

regulation – in particular the installation of the two existing reservoirs in the basin on the Wynoochee and Skookumchuck Rivers. All data were cropped to the start of the first full water year and the end of the last full water year in each record, both for consistency with the hydrologic modeling and to ensure uniform sampling throughout the bias correction procedure.

## 1.7 VIC Hydrologic Model

### 1.7.1 Overview

We used the Variable Infiltration Capacity (VIC) macroscale hydrologic model (Liang et al. 1994, Liang et al. 1996, Gao et al. 2010) implemented at 1/16 degree (Elsner et al. 2010, Hamlet et al. 2013) to produce daily streamflows at sites in or near the Chehalis River (see Table 4). VIC is a physically based, macro-scale hydrologic model which solves the water and energy balance at each grid cell, producing water balance variables (among others) such as runoff, baseflow, evapotranspiration, soil moisture, and snow water equivalent (Figure 11). Downscaled daily meteorological data – precipitation, maximum and minimum daily surface air temperature, and wind speed – were used as inputs to run the VIC model. Additional driving variables such as shortwave radiation, and longwave radiation, and humidity were derived by the model from the primary meteorological inputs.

The VIC model has been widely used to assess the hydrologic impact of climate change on a number of watersheds over the Pacific Northwest and over the western U.S. (e.g., Hamlet et al. 2013). We used the most recent VIC model (version 4.1.2), implemented at the typical resolution of 1/16-degree to simulate hydrologic fluxes (e.g., runoff and baseflow) at each grid cell.

### 1.7.2 Configuration

In addition to daily forcing variables, the VIC uses four parameter files as inputs: the soil parameter file, vegetation file, vegetation library and snowbands parameter file. The soil, vegetation and snowbands parameter files contain information specific to each grid cell while the vegetation library contains general information for vegetation types. We used the parameter files developed/calibrated at 1/16-degree over the Pacific Northwest (Elsner et al. 2010). This section

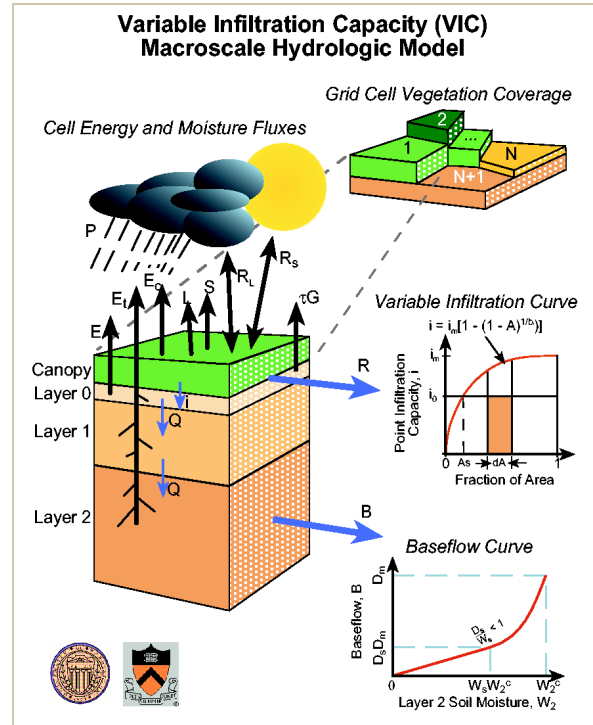


**Figure 11.** Schematic diagram of the land surface representation, and water and energy budgets in the VIC hydrologic model.

briefly describes the contents of each parameter file; additional details can be found in Hamlet et al. (2010).

The soil parameter file contains information such as soil layer depth, infiltration parameter and other soil properties defined by Liang et al. (1994, 1996). The vegetation parameter file used in this study is based on pre-processed parameters from the LDAS (Land Data Assimilation System) dataset for the continental United States, which utilizes a vegetation classification scheme from the University of Maryland (UMD, Hansen et al. 2000) at 1 km spatial resolution. Vegetation data at this scale were aggregated to produce sub-grid proportions of vegetation coverage and associated vegetation parameters at 1/16-degree resolution, all based on the UMD classification scheme. The snowbands parameter file included the sub-grid elevation bands within each VIC model grid cell. The number of elevation bands assigned for a grid cell was based on two criteria: (1) a band may not have a maximum elevation range of more than 500 meters, and (2) there is a maximum of 5 elevation bands allowed per grid cell. For those cells where more than 5 bands would be required to accommodate the 500 meter range limit, the number of bands was set to 5 and the elevation ranges were equally distributed between them. Elevation bands were determined based on a 30 arc-second (about 1 km) Digital Elevation Model (DEM).

### 1.7.3 Streamflow Routing

VIC simulations of runoff and baseflow from each grid cell were used to produce the routed streamflows at each site using a daily-time-step routing model developed by Lohmann et al

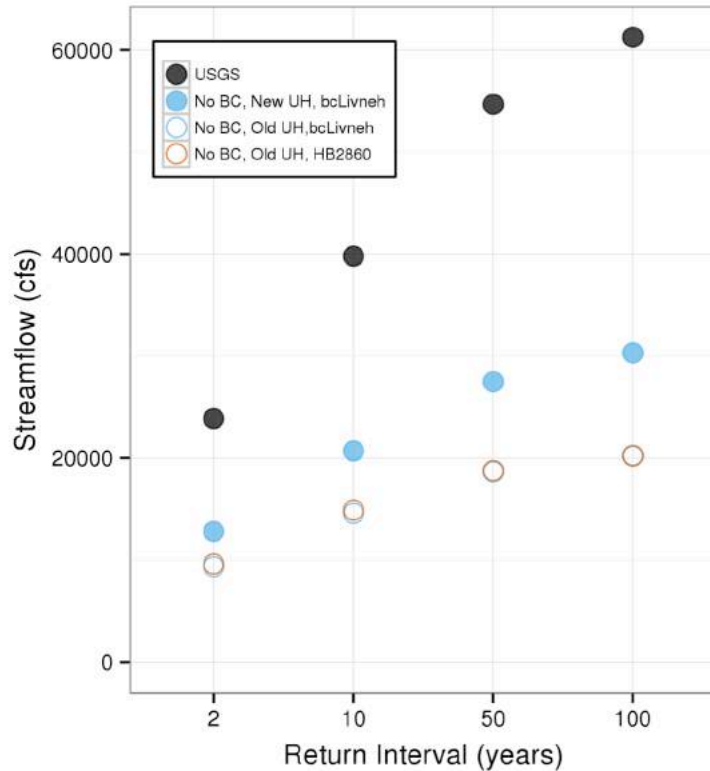


**Figure 12.** Comparing old and new peak flow estimates for the Chehalis River at Grand Mound. Results are similar for old and new historical climate datasets, but the switch to a new unit hydrograph (UH) does reduce biases. The figure compares raw (i.e.: not bias-corrected) peak streamflow observations (USGS) with raw (i.e.: not bias-corrected, “No BC”) model estimates for two input climate datasets – the newer “bcLivneh” (see Table 2) dataset and the older “HB2860” (Hamlet et al. 2013) dataset – and for both a new and old unit hydrograph (“New UH”, “Old UH”), which is used in the streamflow routing. All results stem from VIC hydrologic model simulations, for the years 1950-2006.

(1996). The within cell routing used a Unit Hydrograph (UH) approach to represent distribution of flow at the outlet point with respect to time from an impulse input at each source point and the channel routing used the linearized Saint-Venant equation to represent the flow at a downstream point as a function of the water velocity and the diffusivity, both of which may be estimated from geographical data (Lohmann et al. 1998). The river routing model assumes all runoff exits a cell in a single flow direction.

A predetermined routing network provides the upstream-downstream linkage between VIC model grid cells. The streamflow routing sites described in Table 3 were then located on the developed streamflow routing network and verified based on their true latitude-longitude location and the cited watershed area by the USGS. The routed flows at each site were then bias-corrected to match naturalized streamflow observations using a quantile mapping approach applied to daily flows (see discussion below).

A recent study by Lee et al. (2016) showed that a correction to the unit hydrograph (UH) substantially improved the simulation of high flow extremes. Specifically, the UH was adjusted to distribute runoff more rapidly, whereas the previous formulation had introduced longer delays in flow timing and muted peak flows as a result. We applied the same UH developed by Lee et al. (2016, referred to in the figures as “New UH”). Figure 12 shows that the new UH improves the simulation of flood statistics relative to the previous UH (“Old UH”).

## 1.8 DHSVM Hydrologic model

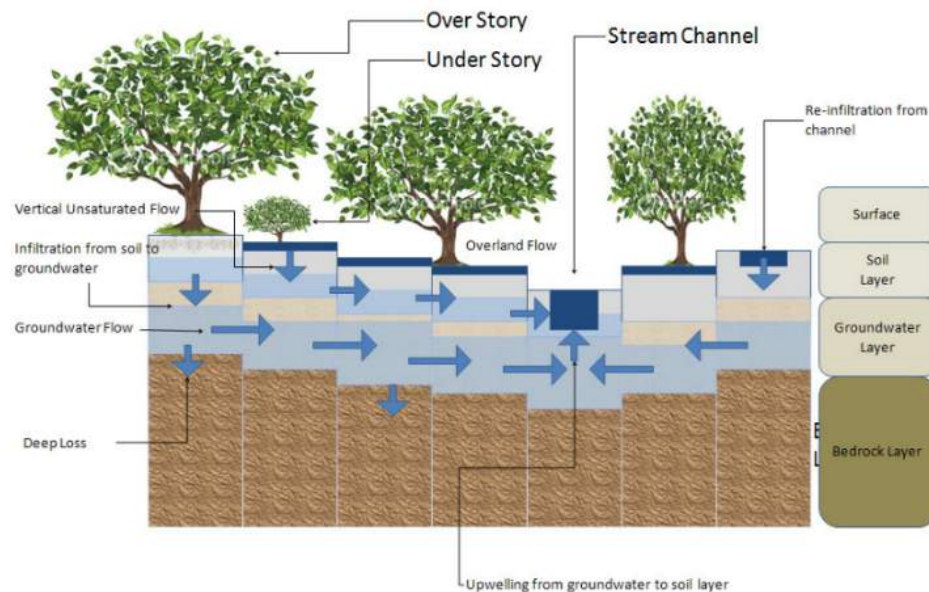


**Figure 13.** Illustration of multi-layer vegetation canopy representation, and vertical and lateral water fluxes within each grid cell of the DHSVM model (Figure based on Wigmosta et al. 2002).

As a high-resolution complement to the VIC model simulations, we used the Distributed Hydrology Soil and Vegetation Model (DHSVM). With its a finer spatial resolution of 150 m (490 ft), the model can capture some of the local scale differences in topography, soils, and vegetation that make up the many tributaries of interest in the Chehalis River Basin. In particular, DHSVM is able to resolve a number of smaller basins on the order of 1 km<sup>2</sup> which cannot be explicitly represented by VIC. This section describes the configuration, testing, and streamflow outputs developed from DHSVM simulations.

### *1.8.1 Overview*

DHSVM is a gridded, spatially distributed hydrology model that represents physical processes of watersheds, incorporating characteristics such as topography, land cover, soil type, soil thickness, and a streamflow network for internal flow routing (Figure 13, Wigmosta et al. 1994, 2002). DHSVM is designed to simulate the spatial distribution of soil moisture, snow cover, evapotranspiration and runoff using a two-layer canopy energy balance model for snow accumulation and melt (Anderson, 1968), a three-layer unsaturated soil model, and a saturated subsurface flow model (Storck et al. 1998) with a mass balance components for snow accumulation and ablation and water from snowpack (Wigmosta et al. 1994) and energy balance representing net radiation, sensible and latent heat transfer, and energy advected by free water (rain, throughfall, drip). DHSVM has been widely applied in the mountainous western United States (e.g., Storck et al. 1998, Bowling and Lettenmaier, 2001, Whitaker et al. 2003, Thyer et al. 2004, Jost et al. 2009) and for assessing the impacts of climate change (e.g., Elsner et al. 2010, Cuo et al. 2011, Cristea et al. 2014, Naz et al. 2014) and land use (e.g., Sun et al. 2013, Cuo et al. 2009, 2011) on streamflow.

### *1.8.2 Model Domain*

The DHSVM model was configured to cover the Upper and Lower Chehalis basins (Hydrologic Unit Codes, or HUCs 17100103 and 17100104). These do not include areas draining to the estuary downstream of Aberdeen. Figure 14 shows the delineation of the full model domain, along with the 55 sub-basin areas delineated to show the direct contributing area upstream of each of the 55 locations of interest (Table 4). The area extends into the Olympic National Forest to the North, the Willapa Hills to the South, and Onalaska to the East.

In DHSVM, the watershed is subdivided into a uniform square grid of cells, or model elements, with spatial resolution generally ranging between 10 m and 150 m; for this study we use a resolution of 150 m. The spatial distribution of the soil and vegetation characteristics of the watershed are captured at the scale of the 150 m Digital Elevation Model (DEM) used as a primary input to DHSVM. As discussed below, some features of the stream network were difficult to resolve, even at this resolution, specifically due to (1) inconsistencies in the average downstream directions when elevations were averaged to a 150 m grid, and (2) the close

vicinity of headwater gridcells at sub-watershed boundaries. . Terrain analysis methods for digital streamflow network and watershed delineation (available in ArcGIS) were used to resolve the spatial distribution of elevation characteristics at the 150 m scale using flow pathways developed at the 30 m scale.

### *1.8.3 Time step*

DHSVM was run at a 3 hourly timestep. In this project, the outputs are aggregated to daily timesteps for analysis. Since the source climate forcing data for this project is only available at the daily timescale, any analysis at the 3 hourly model outputs would be primarily sensitive to the disaggregation process used to generate DHSVM inputs, as opposed to observed or modeled weather variations at the 3 hourly time scale. In addition, sub-daily flows are much more sensitive to calibration, in particular relating to the timing of runoff and routing through the stream network. Although not feasible in the current project, future work could investigate the potential for using the 3-hourly streamflow estimates.

### *1.8.4 Inputs*

This section describes the development and configuration of the soil, vegetation, and climate inputs to DHSVM. DHSVM is initialized with a series of four state files representing snow, soil, stream channel, and interception storage. In addition, there are a series of constant parameters that are applied uniformly across the entire domain (Table 5).

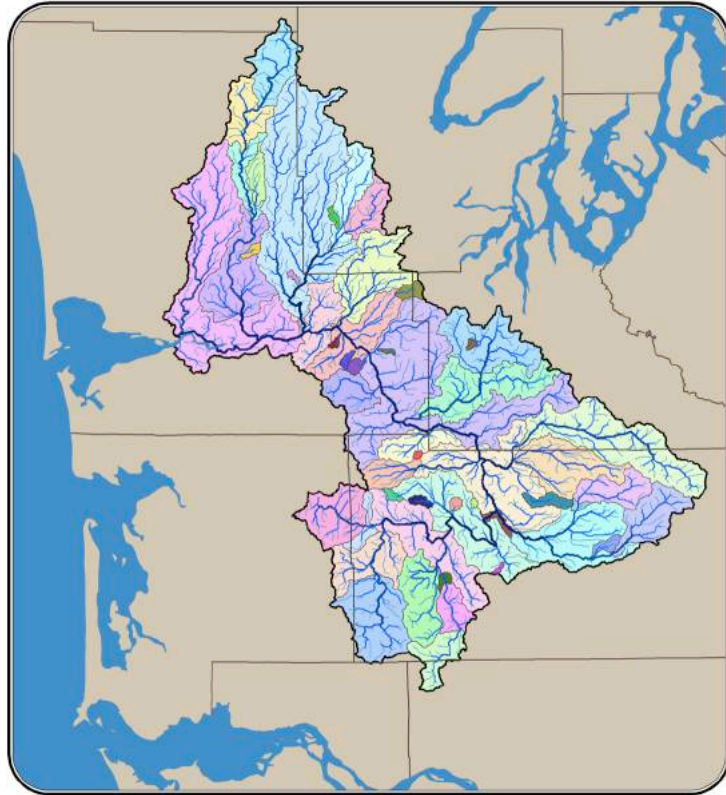


**Figure 14.** DHSVM model domain, digital stream network, and 55 sub-basins with direct contributing area to the 55 model output locations (Table 4). The stream network is classified by Strahler stream order (Strahler 1957), showing increasing thickness as streams progress from the headwaters to the mainstem. For the sub-basins, note that the “direct contributing area” is defined here as the contributing basin area that is unique to each specific site, and that the full contributing area will often be larger since many sites include smaller upstream tributaries that are also among the 55 model output locations.

**Table 5.** Constant Parameters used in Chehalis Basin DHSVM

Constant Parameter Description	Value	Source
Roughness of soil surface	0.02 (m)	Frans, 2015
Roughness of snow surface	0.01 (m)	Frans, 2015
Rain threshold: Minimum temperature at which rain occurs	0.5 (°C)	Dai, 2008
Snow threshold: Maximum temperature at which snow occurs	0.03 (°C)	Dai, 2008
Vegetation reference height	70 (m)	Frans, 2015
LAI Multiplier for rain interception	0.0001	Czarnowski and Olszewski, 1968
LAI Multiplier for snow interception	0.0005	Storck, 2000
Intercepted snow that can only be melted	0.005 (m)	Storck, 2000
Temperature lapse rate	-0.0055 (°C/m)	Minder et al. 2010
Precipitation Lapse Rate	0.001 (m/m)	Henn et al. 2015
Maximum Snow Albedo	0.878	Frans, 2015
Precipitation Multiplier	1	Calibration parameter

#### 1.8.4.1 Land cover

The land cover information was developed using the National Land Cover Database 2011 (NLCD 2011; Figure 15, Table 6). This is the most recent national land cover product, with a 16-class land cover classification scheme applied at a spatial resolution of 30 meters based on circa 2011 Landsat satellite data and created by the Multi-Resolution Land Characteristics Consortium (Homer et al, 2015).

In the current configuration, the root zone parameter ranges in depth from 0.19-0.22 meters. Developed classes were parameterized with a leaf area index (LAI) ranging from 1.0 in the winter and 3.0 in the summer and an albedo of 0.2. Deciduous forest LAI ranged from a minim of 0.14 in January to a maximum of 5.9 in August, with corresponding monthly albedo ranging from 0.16 in the winter and 0.07 in the summer, and tree height of 30 m. Evergreen forest LAI was

**Table 6.** Vegetation Parameters used in Chehalis DHSVM

Parameter Description	Value range
Vegetation Description	See Figure 12
Impervious Fraction	0-1
Overstory Present	TRUE/FALSE
Understory Present	TRUE/FALSE
Fractional Coverage	default
Hemi Fract Coverage	default
Trunk Space	default
Aerodynamic Attenuation	default
Radiation Attenuation	default
Max Snow Int Capacity	default
Snow Interception Eff	default
Mass Release Drip Ratio	default
Height	0-35
Overstory Monthly LAI	0.1-6
Understory Monthly LAI	0.1-0.5
Maximum Resistance	3000-5000
Minimum Resistance	200-500
Moisture Threshold	0.13-.33
Vapor Pressure Deficit	4000
Rpc	0.108
Overstory Monthly Albedo	0.09-0.16
Understory Monthly Albedo	0.2
Number of Root Zones	3
Root Zone Depths	0.02-0.1
Overstory Root Fraction	0.2-0.4
Understory Root Fraction	0-0.6

a consistent 5.8 throughout the year, with tree height of 35 meters. We referred to Kelleher et al. (2015) to verify that other (less sensitive) parameter values such as maximum snow interception capacity (e.g. Evergreen = 3%), minimum resistance, moisture threshold, vapor pressure deficit, and other land cover related parameters were within physically reasonable ranges.

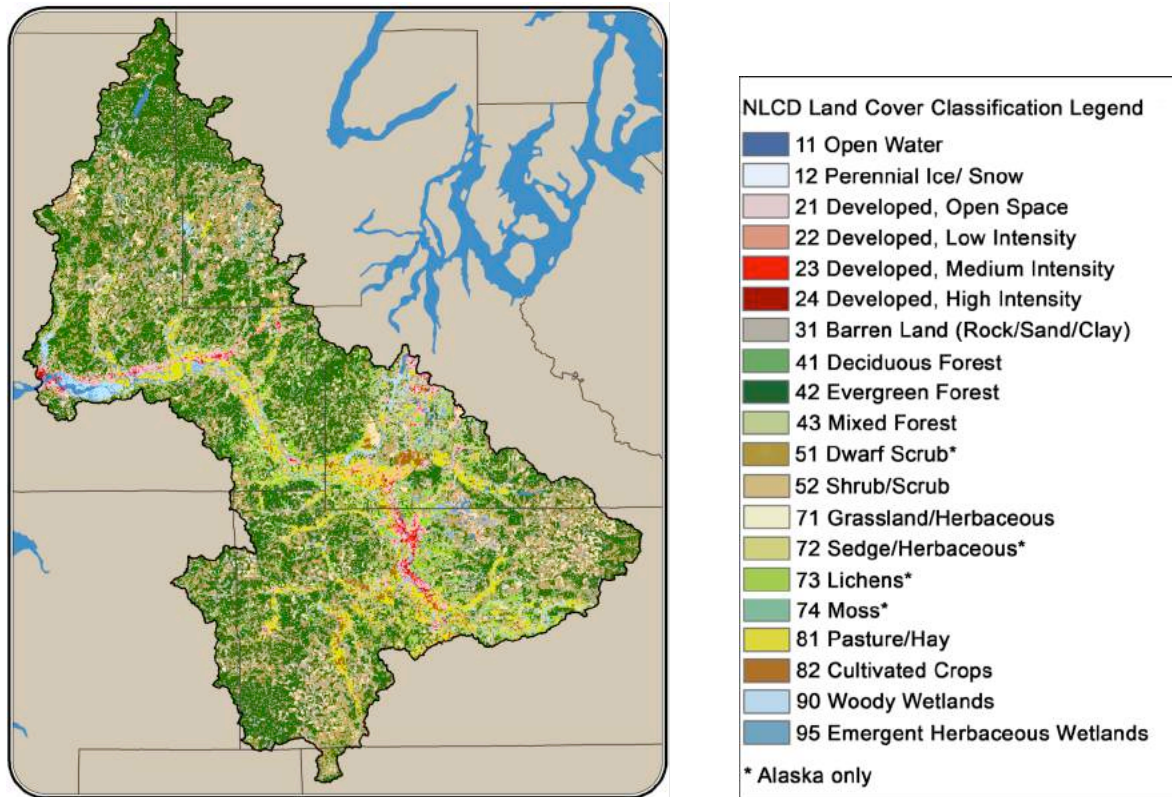


**Figure 15.** Land Cover classification (NLCD 2011) for the Chehalis Basin (classes labeled with \* do not occur within this basin).

#### 1.8.4.2 Soils

The Digital General Soil Map of the United States, or STATSGO dataset (Soil Survey; see references) was developed for regional and national studies designed for broad planning and management uses requiring estimates of soil characteristics. The soil units are distributed as spatial and tabular datasets. The geospatial data maps soil units on a 1-kilometer resolution grid for the conterminous United States by weighting average soil values computed by aggregating soil layers and components of the SSURGO soil database comprised of detailed county soil survey maps. For comparison, the STATSGO database resolves 18 different soil map units from which DHSVM soil parameters can be derived (Table 7; see Kelleher et al, 2015 for parameter value sensitivities, ranges, and references); the SSURGO database resolves 555 unique soil map units. At this time, the maximum number of unique soil types that can be modeled in DHSVM is

256 soil types. As DHSVM is actively used and developed for research, we expect that this functionality will be expanded in future versions of DHSVM.

Although vegetation and soils data are derived from two different sources, physical consistency must be maintained between the depth of soil and depth of roots. In DHSVM, the rooting depth (specified in the vegetation parameters) cannot exceed the soil depth (specified in the soil depth grid); for this reason, the soil depth was limited to 0.75-2.5 m deep based on the STATSGO soil depth range of 0.08 – 1.75 m and the estimated minimum rooted depth of evergreen trees of 0.5 m.

**Table 7.** Soil Parameters used in Chehalis DHSVM

Parameter Description	Value range
Soil Description	See Figure 14
Lateral Conductivity (m/s)	0.01-0.00015
Exponential Decrease (1/m)	0.7-3
Maximum Infiltration (m/s)	0.00001
Depth Threshold	0.5
Capillary Drive	0.1
Surface Albedo	0.1
Number of Soil Layers	3
Porosity	0.39-0.52
Pore Size Distribution	0.08
Bubbling Pressure	0.29
Field Capacity	0.31
Wilting Point	0.23
Bulk Density (kg/m <sup>3</sup> )	1565
Vertical Conductivity (m/s)	0.01
Thermal Conductivity (W/m <sup>2</sup> °C)	6.9-7.1
Thermal Capacity (J/m <sup>3</sup> °C)	1400000
Mannings n	0.013

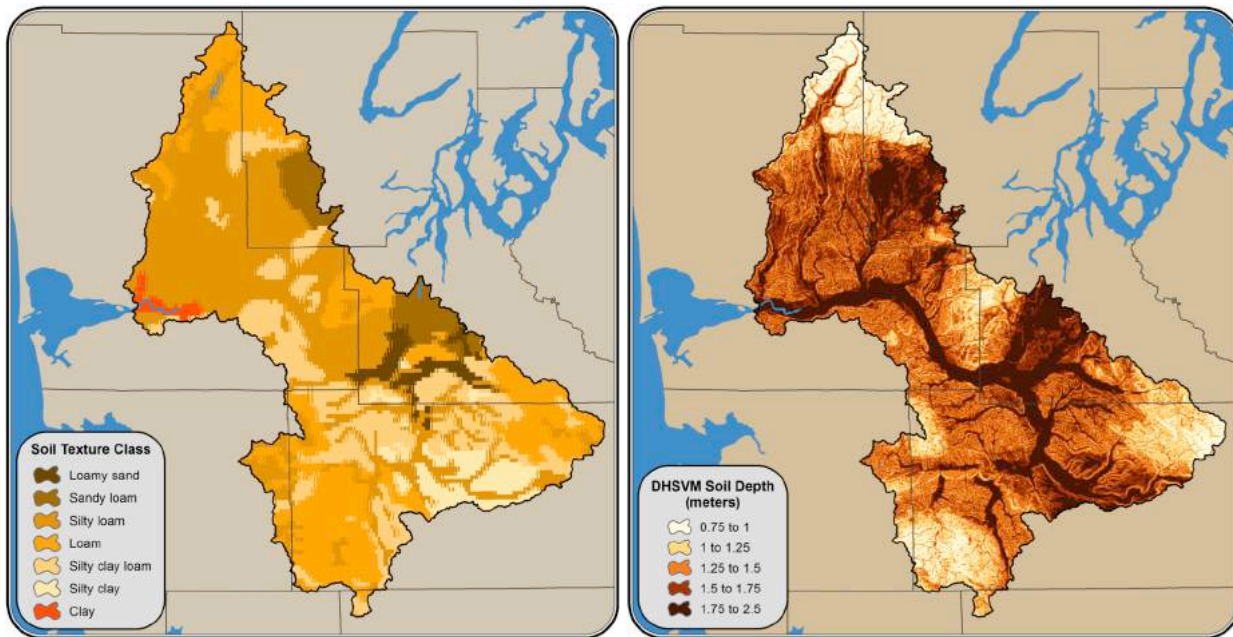


**Figure 16.** STATSGO soil types (left) and soil depth (right) derived from the Chehalis basin topography.

### 1.8.4.3 Meteorological Forcings

Six variables in 3-hourly timesteps are required to run DHSVM: Temperature ( $^{\circ}\text{C}$ ), relative humidity (%), precipitation (m), wind speed (m/s), and incoming shortwave and longwave radiation ( $\text{W}/\text{m}^2$ ). As a pre-processing step, we used the VIC model to disaggregate the daily meteorological data to a three-hourly time step, and to estimate humidity and radiative fluxes. In VIC, solar radiation, longwave radiation, and relative humidity are estimated following Thornton and Running (1999) and Bohn et al. (2013).

In this study, meteorological inputs were provided at the 8 points shown in Figure 15. These were selected for computational feasibility: with the 8 model input points, a 100-year model run takes about 5 days to complete on UW's High Performance Computing cluster, whereas the full resolution 1/16-degree data (229 grid cells) would require 3 weeks. Given the large number of simulations (over 1000 years of simulations) used in this study, it was not feasible to use the full resolution inputs to DHSVM. Future work could explore different approaches to parallelization, which may lead to more efficient processing.

The eight grid cells correspond to the grid cell closest to the centroid of each of the 8 major sub-basins of the Chehalis: Wynoochee, Satsop, Cloquallum, Black, South Fork Chehalis, Skookumchuck, Newaukum, and Elk. These 8 input points are interpolated to each 150 m DHSVM grid cells using the Mountain Microclimate Simulation Model (MTCLIM; Hungerford et al. 1989, Kimball et al. 1997, Thornton and Running, 1999, Thornton et al. 2000, Bohn et al. 2013). An assumed precipitation lapse rate is used in the disaggregation (Table 5). Sensitivity tests showed moderate sensitivity to the choice of a lapse rate, indicating that 0.001 m/m resulted in better simulations of peak flows.

DHSVM requires spatial information for each point included as an input time series, with latitude and longitude in UTM coordinates (Zone 10, WGS84) and elevation in meters. To run the model, the input file lists each grid cell in the following format:

```
Station Name 1 = data_46.53125_-123.28125  
North Coordinate 1 = 5153114.279000  
East Coordinate 1 = 478431.528300
```

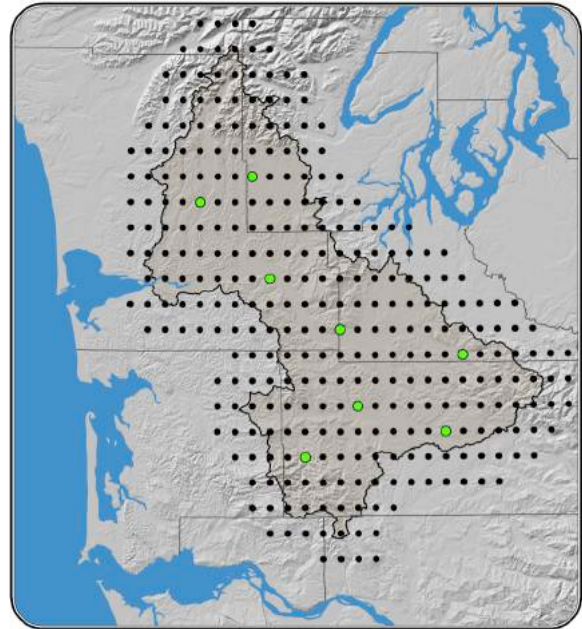


**Figure 17.** Meteorological input locations for DHSVM (green), and full 1/16-degree grid (black). The Chehalis basin is outlined for reference.

Elevation 1 = 290  
Station File 1 =  
/civil/shared/eco hydrology/christina/forcs\_dhsvm/data\_46.53125\_-  
123.28125

The steps required to calculate this information are outlined in the HydroShare resource entitled “Chehalis Basin Climate DHSVM spatial processing” (see Appendix).

#### 1.8.4.4 Streamflow network

DHSVM routes streamflow using flow direction relationships between upstream (higher elevation) and downstream (lower elevation) grid cells. The model stream network and watershed boundaries are derived in a pre-processing step, based on a digital elevation model (DEM, *Data available from the U.S. Geological Survey*) developed at the resolution of the model grid. The result is a stream network that accurately routes contributing areas to downstream model locations of interest, though the computed digital network may vary from the actual network due to the limitations of model resolution. Figure 11 shows the Chehalis Basin DHSVM digital network classified by Strahler stream order, illustrating how headwater streams (thin blue lines) have connectivity to larger streams and ultimately the mainstem Chehalis River (thick blue lines).

The goals of this process are to (1) have the entire basin drain to one outlet, (2) develop a continuous connected network, and (3) ensure the correct drainage area to each model output location. One challenge of delineating a digital network using a 150 m DEM is that the flow directions derived from a 150 m average elevation do not always generate flow pathways that match the actual landscape, especially in terrain with low relief, or where streams curve at low elevation valleys next to higher elevation topography. To address this, we first developed a stream network using a 30 m DEM, and used this to modify the 150 m DEM to ensure that the flow directions were correctly represented. This involved an iterative process of adjustments to the 150 m DEM and comparisons with the 30-m and NHDplus river network (McKay et al. 2012).

## Post-processing

---

### 1.9 Model spin-up

Prior to post-processing, all streamflow simulations must be adjusted to remove the model spin-up time. Tests with varying start dates indicated that the sensitivity to initial conditions was nearly undetectable after just a few months of run time. As a conservative guard against biases arising from model spin-up, we discarded the first 9 months of all model simulations.

## 1.10 Daily bias-correction

Since the current scope did not include time for calibration of the hydrologic models, bias correction was used to adjust streamflow estimates to reflect flows recorded in the observations. In previous approaches bias correction was applied at monthly time scales – adjusting naturalized streamflow using a quantile mapping approach outlined by Snover et al. (2003). A primary concern in monthly bias correction is that biases in the sub-monthly distribution of streamflow – daily flows, in particular – will not be removed in the process.

Given the emphasis on daily extremes in this study, a daily bias-correction approach was developed. To do this, we adapted the statistical downscaling methods used to develop the MACA dataset (Abatzoglou and Brown 2012, Hegewisch and Abatzoglou 2016, described above) for use with observed and simulated daily streamflow estimates. The method works as follows:

1. Remove the long-term trend, estimated using a 45-day/31-year moving average. Estimate anomalies using a multiplicative scaling, by dividing raw flows by the long-term trend.
2. Scale the long-term trend – in both historical and future simulations – based on the ratio of the mean in the historical simulation to the mean of the observations.
3. Bias Correction:
  - a. Looping through each day of the year, select daily flows using a 45-day window applied to the full record of observations and historical and future simulated daily flows
  - b. Bias-correct the daily anomalies by mapping quantiles from the observed and simulated flows selected in the previous step.
  - c. Preserve future changes relative to historical by mapping quantiles from simulated historical and future flows.
4. Recombine by multiplying the scaled estimates of the long-term trend with the bias-corrected anomalies.

The 31-year moving window was selected to as a compromise between adequate sampling of long-term variability and accurate estimation of long-term trends. Similarly, the 45-day window was chosen in order to encompass a range of seasonally-representative conditions yet avoid conflating short-term variations with seasonal variations in flow conditions, since the mechanisms (and therefore probability distributions) for each may not be the same. Tests indicate that the results are not particularly sensitive to the exact choice of window width, but that much shorter windows can lead to biases due to limited sampling and mis-matched seasonalities among observed and simulated streamflows.

Since the long-term trend has already been removed, bias correction can be applied to the full daily record of simulated historical and future streamflow. Step 3(c) is needed because changes

in extreme flows may not scale with changes in the 45-day/31-year average: the quantile mapping preserves the changes in extremes that are exhibited in the raw simulations.

Tests show that all bias-correction approaches lead to substantial improvements in estimates of flow extremes, but that the daily approach is superior, especially for estimating the magnitude of the 10-, 50-, and 100-year peak flows (Figure 15).

## 1.11 StreamFlow Statistics

### 1.11.1 Time periods

Monthly averages and extreme statistics were calculated for three 30 year time periods: 1970-1999 (“1980s”), 2040-2069 (“2050s”), and 2070-2099 (“2080s”).

Although longer time periods might be desired to estimate extreme statistics, 30 years was deemed an appropriate compromise between longer periods, which may conflate long-term changes in flood risk with increased sampling of the extremes, and shorter time periods, which can limit the reliability of extremes estimates.

### 1.11.2 Extreme Flows

To calculate extreme statistics, the Extreme Value type 1 distribution described Gumbel (EV1), the Log-Pearson type 3 (LP3) and the generalized Extreme Value (GEV) distribution with L-moments are commonly used. In this study we apply the GEV distribution with L moment to estimate flood and low flow statistics – following the methodology described in Salathé et al. 2014 and Tohver et al. 2014 – based on findings that indicate it is superior to the LP3 distribution (Rahman et al. 1999 & 2015, Vogel et al. 1993, Nick et al. 2011). Flood flows were computed for return intervals of 2, 10, 50, 100 and 500 years. To estimate flood magnitude, the maximum daily flows were extracted for each water year (October to September) at each site.

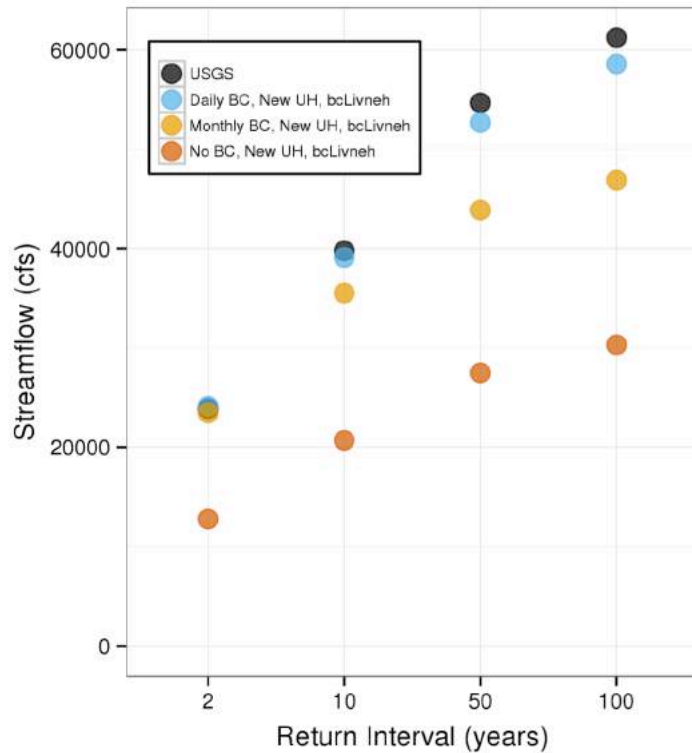


**Figure 18.** Daily bias correction results in significantly improved peak flow estimates. Results are shown for the Chehalis River at Grand Mound, comparing observed (USGS) peak flow to those estimated from raw (No BC), monthly bias-corrected (monthly BC), and daily bias-corrected (daily BC) simulations. All simulations are based on the bcLivneh (see Table 2) historical dataset and VIC hydrologic model, evaluated for water years 1950-2013.

These were ranked for each 30-year period and fitted to the GEV with L-moments (Wang 1997, Hosking and Wallis 1993, Hosking 1990).

The lowest consecutive 7-day flows with a 2- (7Q2) and 10-year return interval (7Q10) were also estimated as a measure of extreme low flows. For the extreme low flow analysis, the same procedure used for estimating flood magnitude was followed, except the minimum 7-day consecutive running average streamflows were selected for each water year in lieu of maximum daily flows.

### 1.12 Data structure

All results, model files, climate data, and other documentation are linked from main project page (resources, with links, are listed in Appendix A).

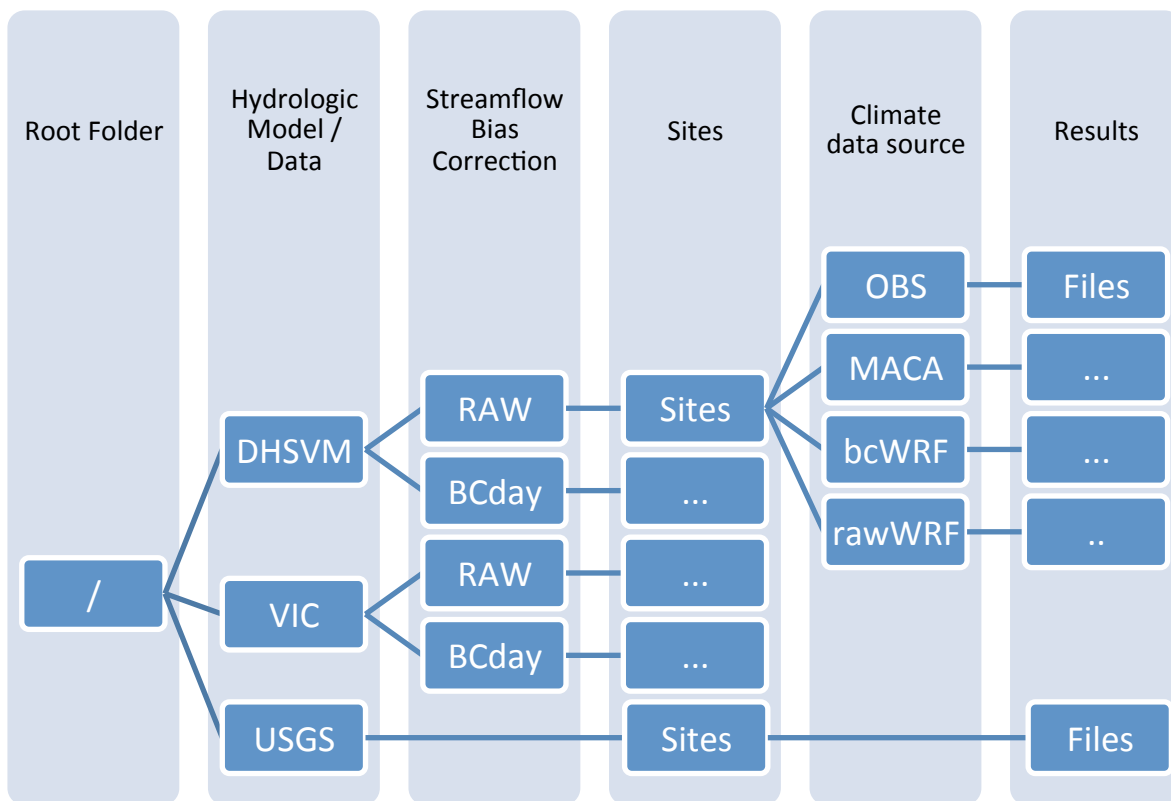


**Figure 19.** Data structure for streamflow results.

**Table 8.** File organization and naming.

<i>File Type</i>	<i>Time Series Files</i>	<i>30-year Average Files &amp; Graphics</i>
<i>Site Name</i>	(see Table 3)	
<i>Climate Data</i>	(see Table 2)	
<i>Time Range</i>	<i>MACA:</i> historical-full RCP45-full RCP85-full  <i>WRF:</i> historical-full SRES-A1B-full	<i>MACA:</i> historical-1980s RCP45-2050s RCP45-2080s RCP85-2050s RCP85-2080s  <i>WRF:</i> historical-1980s SRES-A1B-2050s
<i>Hydrologic Model / Data</i>	VIC / DHSVM / USGS	
<i>Bias Correction</i>	Raw / BCday	
<i>Data Type</i>	DailyFlows MonthlyFlows LowFlows PeakFlows	MonthlyAvg LowStats PeakStats

### 1.12.1 *Streamflow data*

Historical and future streamflow estimates were produced for two hydrologic models (VIC and DHSVM), both with and without streamflow bias correction, four climate datasets (bcLivneh, MACA, bcWRF, rawWRF; Table 2) – for which there are results for a total of 12 different global climate models, three greenhouse gas scenarios (SRES A1B, RCP 4.5, RCP 8.5), and three separate time periods (1970-1999, 2040-2069, and 2070-2099) – and 59 streamflow sites.

The streamflow data are organized following the structure shown in Figure 16, where each column in the figure denotes one directory tier. Within each results directory (right-hand column in Figure 16), there are three types of files: time series files, 30-year averages, and graphics (Table 6). Time series files are provided for the entire available data set and labeled as ‘full’. These include the time series of daily flows (‘DailyFlows’), monthly average flows (‘MonthlyFlows’), annual 7-day low flows (‘LowFlows’), and the annual max of peak daily flows (‘PeakFlows’). Three types of data are provided for the 30-year averages: low and peak flow return statistics (LowStats/PeakStats), and the average monthly flows for each calendar month (MonthlyAvg). As with the time series files, separate versions of these files are created for each greenhouse gas scenario and each time period (1980s, 2050s, 2080s). In addition to the

data files, plots were created for each of the three the 30-year average results to facilitate quick looks at the results. The naming convention for all data files is as follows:

<Site Name>\_<Climate Data>\_<Time Range>\_<Hydro. Model / Data>\_<Bias Correction>\_<Data Type>.csv

The naming associated with each of these files is listed in Table 8.

## Task 1 Results: Evaluating Changes in Rainfall

---

Previous studies have shown that ARs are the dominant physical mechanism associated with heavy rainfall in the Pacific Northwest region (e.g., Ralph et al. 2006, Dettinger et al. 2011, Warner et al. 2012). Studies have also suggested that ARs will carry more water vapor in the future in association with a warming climate (e.g., Warner et al. 2015), and that the mid-latitude storm track will shift northward (IPCC, 2013). Other aspects of intense winter storms may have specific implications for the Chehalis, for example by altering how the storms interact with the topography of the basin. In this analysis, we address the following questions:

1. Will future ARs result in more intense precipitation in the Chehalis?
2. Will there be a change in the distribution of precipitation over the basin?

### 1.13 WRF precipitation Projections

Consistent with previous studies (e.g., Warner et al. 2015), WRF projects an increase in the intensity of heavy rain events (Figure 20). Specifically, all quantiles examined (80<sup>th</sup>, 90<sup>th</sup>, 95<sup>th</sup> and 98<sup>th</sup> percentile values) showed an increase in total daily precipitation, on average, for both the entire basin and the area upstream of the proposed dam, for the middle of the 21<sup>st</sup> century

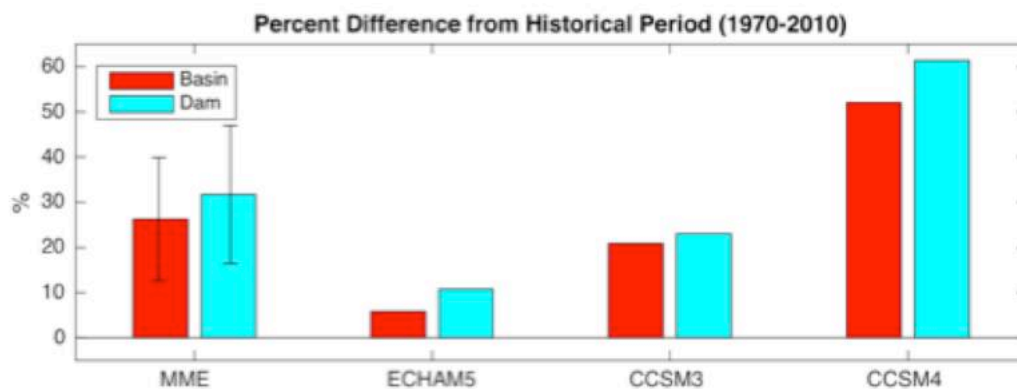


**Figure 20.** Projected change (%) in the 98<sup>th</sup> percentile of daily precipitation, for 2030-2070 relative to 1970-2010. Based on the three WRF climate change projections described in Section 1.4.2. MME stands for multi-model ensemble.

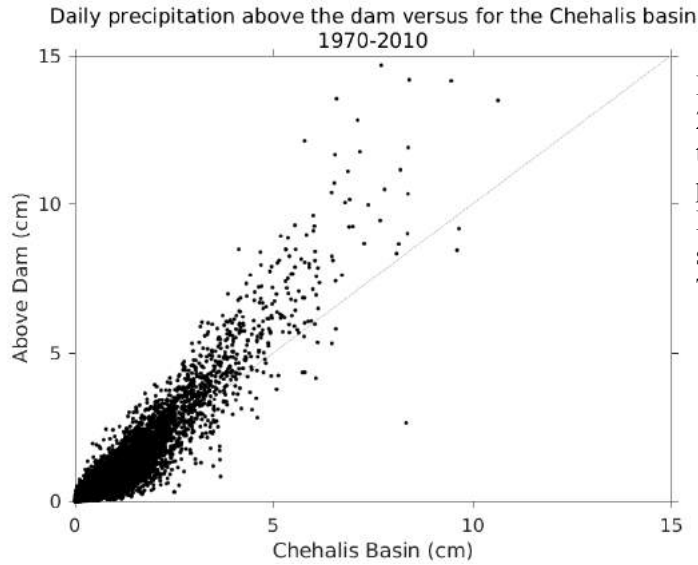


**Figure 21.** Scatterplot of historical (1970-2010) daily simulated precipitation above the proposed dam vs. the average precipitation for the entire Chehalis basin. Each dot represents the results for one single day out of the full 41-year period. The 1:1 line is shown in gray.

(2030-2070) relative to historical (1970-2010). The 40-year time periods, as opposed to 30-year averages, were chosen in order to obtain better estimates of the extreme values.

Figure 21 shows that there is generally a very close match between precipitation above the proposed dam and the average accumulation for the basin as a whole. Although there is some indication that the large events are associated with a greater proportion of rain above the dam, it is not clear if this is simply due to the positioning of storm systems – which may overlap with the southern portion of the basin but not the northern portion – or due to a mechanism driving increased intensities in this portion of the basin.

A primary motivation for this study was to investigate the potential for climate change to alter the distribution of heavy rainfall across the basin. Figure 22 shows the change (in %) in the

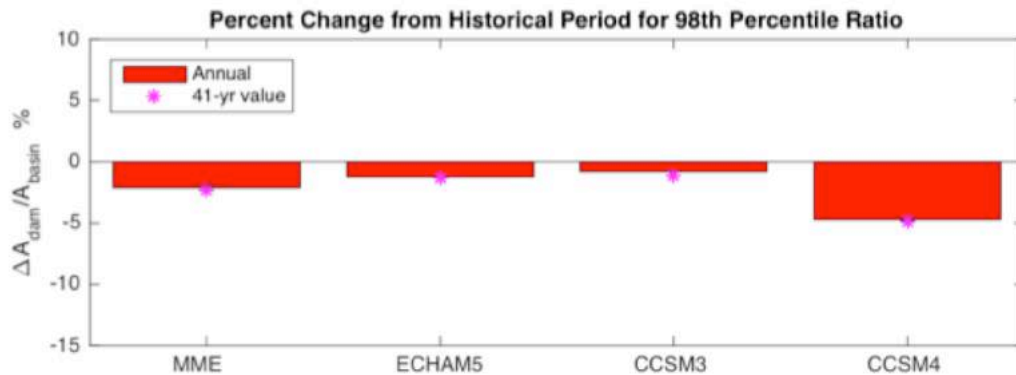


**Figure 22.** Projected change (%) in the ratio of precipitation above the dam vs. the entire Chehalis basin. Results are shown for a 98<sup>th</sup> percentile rain event, for 2030-2070 relative to 1970-2010. The 98<sup>th</sup> percentile is calculated both as an average of the values for each individual year (red bars) and for the entire 41-year record (asterisks).

proportion of rain falling upstream of the proposed dam relative to the Chehalis basin overall. The projections show a small decrease in the proportion of rain falling above the dam, but the changes are small compared to intermodal differences and unlikely to result in significant changes in the distribution of flood risk across the watershed.

### 1.14 Assessing the drivers of Heavy precipitation

Additional information may be gained by examining the large-scale weather patterns associated with heavy precipitation events and evaluating whether or not these patterns are projected to change.

We examine the daily rain rate and

IVT associated with each mode by regressing the full fields onto the combined or complex EOFs for each mode (see “Climate Data & Models” section for details on the approach).

The EOF analysis was applied separately to the global model IVT data based on 90<sup>th</sup> percentile precipitation events for each of the historical WRF simulations (NNRP, ECHAM5, CCSM3, and CCSM4). Each set of EOFs consistently showed two leading modes of variability (Figure 23). The dominant mode shows the typical pattern one might expect for these events, with southerly or southwesterly flow associated with a mid-latitude cyclone intercepting the coastline, while the second shows the alternate configuration, in which the flow is influenced by anti-cyclonic circulation also associated with a wave in the jet stream (referred to as Rossby waves). Both are well-known atmospheric river event configurations for the Pacific Northwest (Ryoo et al. 2013). There is also a third pattern (not shown) that appears distinguishable from the noise in some analyses, and which may be associated with a smaller cyclone breaking downstream of a larger system over the Pacific – this third mode would require more study to understand its development. Although all analyses show the same sequencing among the first few modes, the decrease in variance explained for the 2<sup>nd</sup> and 3<sup>rd</sup> modes is greater for the global model simulations (ECHAM5, CCSM3, CCSM4) than for the observationally-based reanalysis

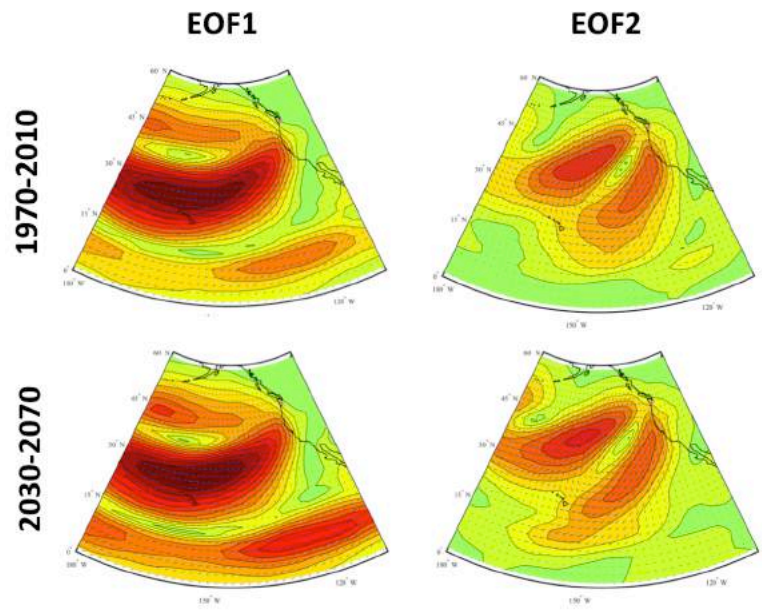


**Figure 23.** Composite anomaly in integrated vapor transport (IVT) for the 1<sup>st</sup> and 2<sup>nd</sup> modes identified in the EOF analysis. Results are shown for the ECHAM5 model for historical (1970-2010) and future (2030-2070); similar patterns were found for the other WRF simulations. No color scale is shown because these are normalized anomalies: red shading indicates above average conditions, while the light green shading indicates average conditions. Wind vectors are denoted with arrows.

simulation (NNRP). In all analyses, the first mode explained about 10-20% of the variability, while the 2<sup>nd</sup> and 3<sup>rd</sup> modes explained about 7-10% of the variability each.

The combined EOF analysis was also applied to the future simulations for the years 2030-2070. These showed the same modes, but with more water vapor transport. This is consistent with previous research (Warner et al. 2015, Scheff et al. 2015), which suggests that changes in precipitation in the Pacific Northwest are primarily driven by the increase in water-holding capacity of warmer air and not with a change in the intensity or position of storm systems. All of these future modes explain a smaller proportion of the variability than in the historical period.

Anomalies in each variable associated with the zonal (east-west) and meridional (north-south) vapor transport (IQU and IQV, respectively) modes must be examined separately in the case of the complex EOF analysis since the phase of their maximum variance differs (Figure 24). This analysis shows that the transport anomalies in the zonal direction are first, followed by the transport anomalies in the meridional direction. To complete a full phase of the wave captured by the complex EOF analysis, the negative of the zonal transport pattern would then occur, followed

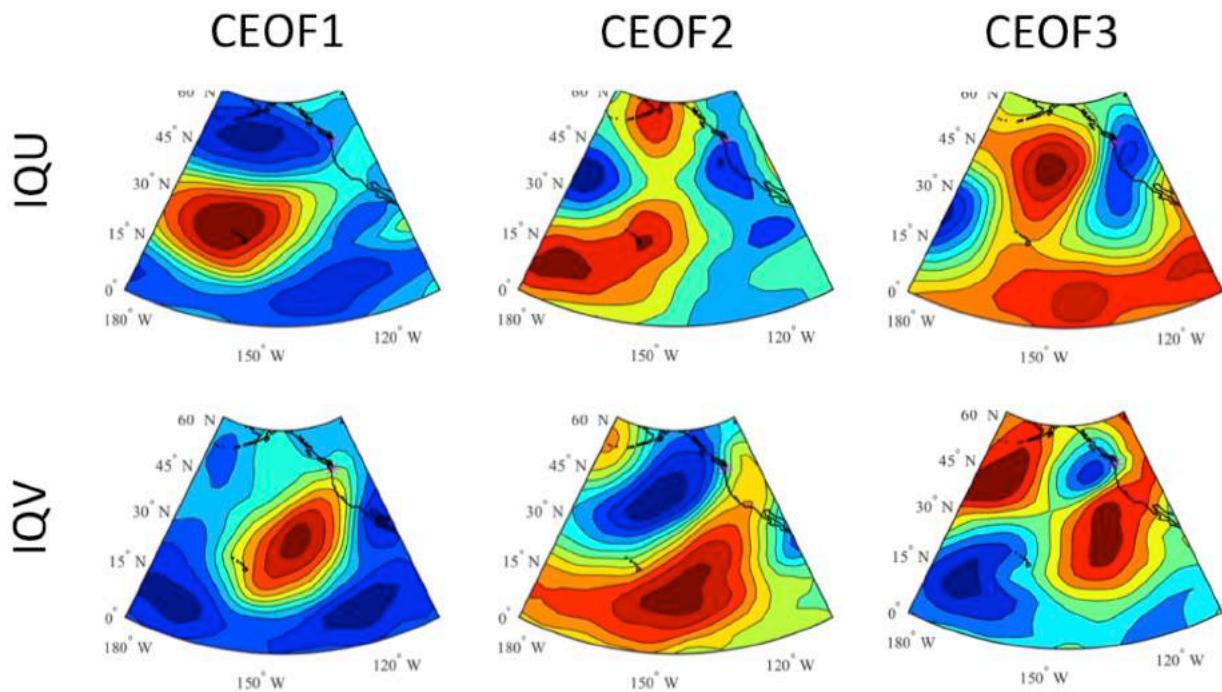


**Figure 24.** Composite anomaly in integrated vapor transport (IVT) for the 1<sup>st</sup>, 2<sup>nd</sup>, and 3<sup>rd</sup> modes identified in the complex EOF analysis. Results are shown for the NNRP simulation model for 1970-2010; similar patterns were found for the other WRF simulations. Since it is a complex EOF, both westerly (IQU) and southerly (IQV) integrated vapor transport are shown for each mode. No color scale is shown because these are normalized anomalies: red shading indicates positive anomalies (anomalous westerly or southerly transport), while blue shading indicates negative anomalies (anomalous easterly or northerly transport).

# NNRP WRF – EOF 1

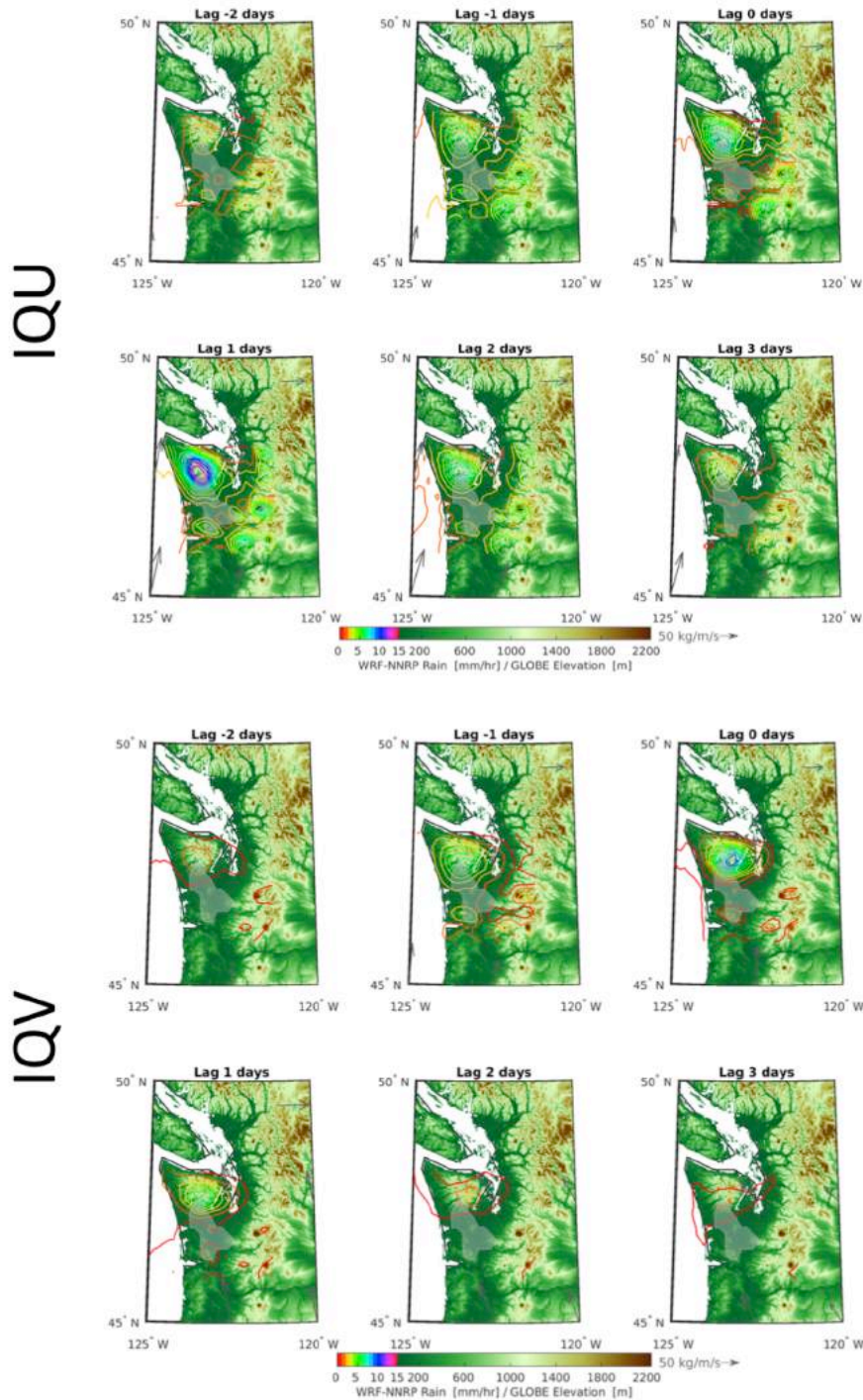


**Figure 25.** Composite maps of lagged precipitation (colored contours) and integrated vapor transport (IVT, gray arrows in lower left of each map) for the leading mode identified in the complex EOF analysis. Results are shown for the NNRP simulation model for 1970-2010; similar patterns were found for the other WRF simulations. Since it is a complex EOF, there are two independent composites: one based on the leading mode in westerly (IQV) and southerly (IQV) integrated vapor transport. The topography of the region is shown via the shading, and the Chehalis basin is highlighted in grey.

by the negative of the meridional transport pattern (only the positive patterns are shown in Figure 24). In the case of the first mode, the anomalous westerly transport anomalies (red) across the Pacific centered on about 20°N accompanied by the anomalous easterly transport (blue) to the north are followed by anomalous southerly transport reaching from south of Hawaii to the west coast of North America. These anomalies describe a mid-latitude cyclone circulation like that seen for the first combined EOF mode in Figure 23. In general, the two leading complex modes correspond closely with those identified in the combined analysis, in addition to a more robust third mode that appears to lack the clear atmospheric river signal seen in the previous two patterns. As with the combined analysis, the global model projections assigned more weight to the leading EOF relative to the reanalysis-based simulation.

Evaluating the time progression of rainfall associated with the complex EOF patterns, maximum rainfall anomalies are observed in association with the westerly vapor transport anomalies a day after the maximum anomalies in the southerly vapor transport (Figure 25). This is consistent with the fact that the westerly vapor transport anomaly maximum over the basin occurs after the low pressure center has arrived onshore, whereas the southerly transport anomaly is a maximum as the storm first arrives at the coast.

For both the combined and complex EOF analyses the primary modes of variability in IVT are associated with an AR event linked to a mid-latitude wave-like structure in the storm track. Neither analysis indicated substantial variation in the angle at which these events intercept the coastline: as shown in Figure 25 (gray arrows, lower left of each map), the moisture transport consistently arrived from the south or south-southwest. However, more study is required to examine the transport vectors in order to fully understand the implications of the transport directional anomalies and precipitation in the basin.

Based on this analysis, the mechanisms driving heavy rain events are not expected to change substantially in the future. However, the projections do show that humidity – TPW (total precipitable water) – is projected to increase across the region, resulting in higher moisture transport associated with these storms. Future work could expand on the metrics evaluated here, in particular looking at transport and other possible factors contributing to heavy precipitation, such as atmospheric stability, and evaluate the potential to optimize regional model simulations (e.g., by increasing the resolution) in order to better capture the mechanisms governing precipitation.

## **Task 2 Results: Projected changes in streamflow**

---

Projected changes in streamflow are consistent with previous studies, generally showing an increase in winter streamflow and flood risk and decreases in summer streamflow and low flows. For the Chehalis, winter increases are a response to increases in winter average precipitation,

---

higher intensity rain events, and to a much lesser extent, decreases in snowpack. Summer flow decreases are likely a result of decreases in summer season precipitation and increases in evaporative demand.

All of the streamflow results, both historical and future, for all model and scenario combinations and all selected metrics, are provided online via the links listed in Appendix A. The data are organized as described above in the Section entitled “Data Structure”. In addition to simple excel-readable data files, we provide plots to facilitate quick views of the results. As an example, Figure 26 shows the results for the Chehalis River at Grand Mound, based on the VIC hydrologic model simulations and the MACA statistically downscaled climate projections. Although the projected changes in streamflow differ across the watershed, these results are representative of the findings for most mainstem sites. The figure shows comparisons of historical and future monthly flows in addition to the 2- and 10-year 7-day low flows, and the 2-, 10-, 50-, 100-, and 500-year peak flow values. The range among projections stems from the 10 global models included in the MACA projections. MACA also includes results for both a low and a high greenhouse gas scenario (RCPs 4.5 and 8.5, respectively, see Table 1). The 100-year flood and 10-year 7-day low flow projections for all scenarios are listed in Tables 9 and 10, respectively, for each of the 11 bias-corrected streamflow sites.

In addition to the fact that peak flows are generally projected to increase, while low flows are projected to decrease, the figure highlights a key challenge associated with the interpretation of these results: there is a wide range among projections. In fact, when considering results from both hydrologic models (VIC, DHSVM) and all scenarios (RAW-WRF, BC-WRF, and MACA) there are many cases in which the range encompasses both decreases and increases. In addition, some projections appear to be implausibly large. For example, the high-end projection for the VIC MACA projection at Grand Mound is for a 233% increase in the 100-year peak flows by the 2050s relative to 1970-1999. Given that the projected increase in heavy rainfall for that same time period is about ten times smaller than this, it seems unlikely that this constitutes a plausible change in peak flows. There are a number of important details to note regarding these issues:

1. *There will always be a range among projections.* These are projections about the future, for which there will always be some uncertainty, given the unknowns about greenhouse gas emissions, natural climate variability, and the earth’s climate sensitivity (warming per unit greenhouse gas emissions). Planning for the future will always require consideration of a range among projections.
2. *Neither hydrologic model was calibrated.* Due to budget limitations and the tight timeline under which these results were produced, it was not possible to calibrate the models. Bias-correction, used in lieu of calibration for this study, could introduce artifacts in the projected sensitivity to climate change.
3. *Extremes estimates are limited by sampling.* The projected changes are calculated using 30-year time periods, chosen as a compromise between including a time frame of

## Chehalis River Near Grand Mound (VIC, MACA)

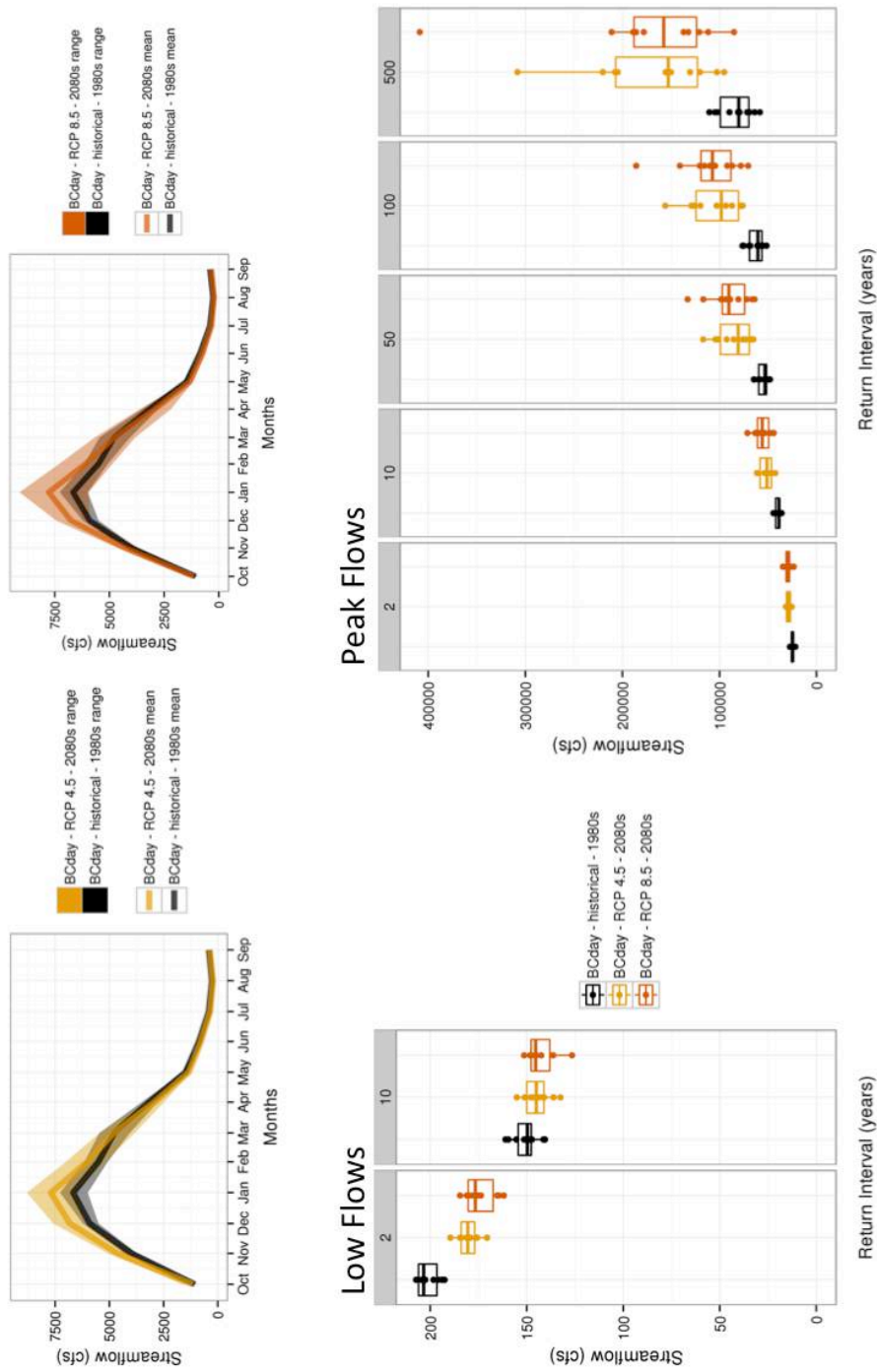


**Figure 26.** Example results for the Chehalis River at Grand Mound, for the 2080s (2070-2099) relative to 1970-1999, based on the statistically downscaled MACA projections and the VIC hydrologic model. The figures show changes for both a low and a high greenhouse gas scenario (RCPs 4.5 and 8.5, respectively), including changes monthly flows (top row) and 7-day minimum flows (bottom left) and peak daily flows (bottom right) for several different return intervals (listed at the top of each plot).

sufficient length for assessing extremes and providing information that does not conflate near-term and long-term changes. This is unlikely to be a major issue for the 2- and 10-year events, and could be partially mitigated by re-computing changes using 50-year time periods. It is almost certainly a source of bias for the 100- and 500-year events.

### Projected Change in 100-year FLOOD for all Bias-Corrected Chehalis streamflow sites

**KEY:** █ ≥+50%: wetter  
█ 0: no change  
█ ≤-50%: drier

#### 2050s:

	rawWRF, SRES A1B			bcWRF, SRES A1B			bcMACA, RCP 4.5			bcMACA, RCP 8.5										
	DHSVM		VIC	DHSVM		VIC	DHSVM		VIC	DHSVM		VIC								
	min	max	min	max	min	max	min	max	min	max	min	max								
ChehalisR-atPorter	-28	16	15	47	-33	23	7	47	20	-21	65	52	-1	225	40	-8	172	76	5	169
ChehalisR-nrDoty	-11	34	-1	45	-15	41	27	29	31	-39	102	38	-29	211	58	-7	135	102	-13	368
ChehalisR-nrGrandMound	7	14	28	96	-9	34	5	55	27	-20	128	54	-5	233	66	10	166	88	22	194
NewaukumR-nrChehalis	49	55	53	128	10	33	53	74	46	-15	230	64	-14	244	85	40	188	91	14	184
SatsopR-nrSatsop	25	59	48	89	15	19	49	131	44	-22	170	71	-32	225	13	-26	47	26	-35	73
SkookumchuckR-blwBldyRunCr	-39	19	-21	7	-46	20	-24	16	24	-42	108	46	-4	238	56	-17	161	65	-5	224
SkookumchuckR-nrBucoda	-27	1	-25	9	-46	17	-30	3	22	-46	105	48	-4	196	40	-10	111	58	-6	169
SkookumchuckR-nrVail	-13	2	-25	27	-41	11	-40	3	27	-37	135	37	-10	199	65	12	131	69	-1	233
WynoocheeR-abvBlackCr	54	69	18	45	18	50	16	86	40	-21	208	63	-24	263	22	-15	47	36	-31	102
WynoocheeR-abvSaveCr	3	57	47	67	-8	43	-4	26	21	-24	94	42	-7	142	22	-18	95	35	-10	118
WynoocheeR-nrGrisdale	20	36	47	87	23	25	-2	89	27	-14	104	31	-9	97	24	-6	63	24	-19	57

#### 2080s:

	rawWRF, SRES A1B			bcWRF, SRES A1B			bcMACA, RCP 4.5			bcMACA, RCP 8.5										
	DHSVM		VIC	DHSVM		VIC	DHSVM		VIC	DHSVM		VIC								
	min	max	min	max	min	max	min	max	min	max	min	max								
ChehalisR-atPorter	--	--	--	--	--	--	--	--	16	-35	68	67	6	189	23	-21	95	76	11	233
ChehalisR-nrDoty	--	--	--	--	--	--	--	--	37	-39	114	82	-4	227	36	-39	147	82	-22	207
ChehalisR-nrGrandMound	--	--	--	--	--	--	--	--	24	-32	82	71	0	171	41	-4	164	79	12	260
NewaukumR-nrChehalis	--	--	--	--	--	--	--	--	36	-11	106	72	-7	198	63	25	160	111	6	228
SatsopR-nrSatsop	--	--	--	--	--	--	--	--	-6	-35	26	12	-37	65	24	-40	64	44	-13	148
SkookumchuckR-blwBldyRunCr	--	--	--	--	--	--	--	--	28	-39	75	39	-16	126	44	-14	113	58	0	161
SkookumchuckR-nrBucoda	--	--	--	--	--	--	--	--	19	-46	66	40	-16	105	46	-6	112	71	20	166
SkookumchuckR-nrVail	--	--	--	--	--	--	--	--	38	-38	110	44	-29	148	58	1	195	69	14	198
WynoocheeR-abvBlackCr	--	--	--	--	--	--	--	--	0	-32	33	20	-22	83	25	-35	97	44	-13	99
WynoocheeR-abvSaveCr	--	--	--	--	--	--	--	--	6	-34	65	23	-15	91	33	-43	123	54	-8	178
WynoocheeR-nrGrisdale	--	--	--	--	--	--	--	--	12	-29	35	17	-17	64	45	-15	102	37	-4	97

**Table 9.** Comparing the projected changes in the 100-year flood for the 11 bias-corrected streamflow sites, for all model/scenario combinations, for the 2050s (top, 2040-2069) and 2080s (bottom, 2070-2099) relative to 1970-1999. For the WRF results, which are based on the moderate SRES A1B scenario (Table 1), results are shown for both the ECHAM5 and CCSM3 projection. Since the WRF projections do not extend past 2070, no results are available for the 2080s. For the statistically downscaled MACA projections, results are shown for both a low and a high greenhouse gas scenario (RCPs 4.5 and 8.5, respectively), and include the average, minimum, and maximum change for all 10 global models. Spreadsheets showing similar results for all return intervals are available for download from the project website.

**KEY:** █ ≥+50%: wetter  
█ 0: no change  
█ ≤-50%: drier

**Projected Change in 10-year LOW FLOW for all Bias-Corrected Chehalis streamflow sites**

**2050s:**

	rawWRF, SRES A1B			bcWRF, SRES A1B			bcMACA, RCP 4.5			bcMACA, RCP 8.5								
	DHSVM		VIC	DHSVM		VIC	DHSVM		VIC	DHSVM		VIC						
	min	max	min	max	min	max	min	max	min	max	min	max						
ChehalisR-atPorter	-22	-16	-18	-16	-20	-15	-3	2	-15	-33	-9	-4	-13	-27	-4	-4	-10	2
ChehalisR-nrDoty	-24	-24	-20	-19	-20	-15	-7	-2	-18	-37	-3	-3	-7	-17	-36	-1	-3	-7
ChehalisR-nrGrandMound	-24	-13	-21	-14	-22	-13	-3	6	-14	-31	-3	-5	-16	-13	-29	-1	-4	-14
NewaukumR-nrChehalis	-20	-11	-16	-13	-21	-12	5	6	-15	-30	-5	1	-13	-17	-33	-3	2	-11
SatsopR-nrSatsop	-33	-16	-22	-16	-25	-14	-13	-7	-23	-39	-10	-14	-21	-26	-40	-6	-15	-24
SkookumchuckR-blwBldyRunCr	-28	-12	-28	-15	-28	-3	-9	4	-17	-45	5	-4	-21	-18	-43	12	-2	-19
SkookumchuckR-nrBucoda	-17	-5	-27	-15	-19	0	4	12	-12	-37	18	-3	-26	-10	-34	27	2	-19
SkookumchuckR-nrVail	-25	-20	-13	-12	-22	-14	-2	-1	-26	-44	-7	-3	-6	-27	-51	-2	-2	-5
WynoocheeR-abvBlackCr	-70	-66	-29	1	-56	-24	-18	4	-47	-72	-10	-19	-32	-48	-73	-21	-17	-38
WynoocheeR-abvSaveCr	-64	-39	-29	-16	-67	-28	-19	-13	-61	-73	-29	-26	-40	-65	-78	-49	-28	-41
WynoocheeR-nrGrisdale	-73	-58	-38	-24	-79	-47	-28	-4	-66	-81	-32	-27	-41	-70	-85	-58	-31	-44

**2080s:**

	rawWRF, SRES A1B			bcWRF, SRES A1B			bcMACA, RCP 4.5			bcMACA, RCP 8.5								
	DHSVM		VIC	DHSVM		VIC	DHSVM		VIC	DHSVM		VIC						
	min	max	min	max	min	max	min	max	min	max	min	max						
ChehalisR-atPorter	--	--	--	--	--	--	--	--	-11	-19	0	-4	-13	-11	-22	2	-5	-14
ChehalisR-nrDoty	--	--	--	--	--	--	--	--	-14	-28	9	-4	-9	-14	-33	0	-4	-10
ChehalisR-nrGrandMound	--	--	--	--	--	--	--	--	-11	-23	3	-4	-15	-11	-30	1	-5	-16
NewaukumR-nrChehalis	--	--	--	--	--	--	--	--	-14	-27	-1	2	-8	-13	-30	1	3	-10
SatsopR-nrSatsop	--	--	--	--	--	--	--	--	-19	-30	-6	-13	-20	-28	-44	-16	-17	-25
SkookumchuckR-blwBldyRunCr	--	--	--	--	--	--	--	--	-15	-35	4	1	-19	-15	-37	4	-10	-28
SkookumchuckR-nrBucoda	--	--	--	--	--	--	--	--	-9	-27	10	4	-10	-5	-29	16	-2	-23
SkookumchuckR-nrVail	--	--	--	--	--	--	--	--	-21	-38	2	-3	-9	-26	-45	-5	-4	-10
WynoocheeR-abvBlackCr	--	--	--	--	--	--	--	--	-51	-85	-17	-23	-53	-61	-76	-48	-32	-42
WynoocheeR-abvSaveCr	--	--	--	--	--	--	--	--	-65	-74	-55	-25	-35	-72	-79	-63	-33	-48
WynoocheeR-nrGrisdale	--	--	--	--	--	--	--	--	-71	-81	-60	-27	-38	-79	-87	-69	-37	-54

**Table 10.** As in Table 9, except showing the change in 7Q10, the 7-day minimum annual flow with a 10-year return interval.

Some of these issues can be diagnosed. For instance, we have made a point of including both raw and bias-corrected streamflow estimates, both for the climate inputs (RAW-WRF vs. BC-WRF) and for the streamflow estimates (RAW vs. BCday), because comparisons among these may be helpful in identifying results that are suspect: bias-correction should not significantly alter the projected change associated with warming.

There are also approaches that can be taken to address many of these issues. Specifically, hydrologic model calibration, undertaken carefully, can ensure that models are more likely to accurately represent both the current state of the Chehalis basin's hydrology, and importantly, its sensitivity to changes in temperature and precipitation. Additional work characterizing the climate drivers of flood risk would also help to better characterize the range among projections. The climate projections used in this study were an "ensemble of opportunity", meaning that they were not optimized for the Chehalis basin. Currently, there simply are not enough WRF simulations available to accurately characterize the range among projections – new regional model simulations could be produced based on a selection of global models that better captures the range among projections for the watershed. In addition, these simulations could be optimized to ensure that the mechanisms governing precipitation change are well represented.

In spite of these issues, the hope is that this dataset will provide a more robust set of results on which to base ongoing assessments and planning decisions. We anticipate an ongoing discussion among managers, scientists, planners, and stakeholders about how to use and interpret this data, along with suggestions on how it could be improved.

## References

---

- Abatzoglou, J. T., & Brown, T. J. (2012). A comparison of statistical downscaling methods suited for wildfire applications. *International Journal of Climatology*, 32(5), 772-780.
- Anderson, E. A. (1968). Development and testing of snow pack energy balance equations. *Water Resources Research*, 4(1), 19-37.
- Bohn TJ, Livneh B, Oyler JW, Running SW, Nijssen B, Lettenmaier DP. 2013. Global evaluation of MTCLIM and related algorithms for forcing of ecological and hydrological models. *Agricultural and Forest Meteorology*, 176, 38-49.
- Borgatti, L., & Soldati, M. 2010. Chapter 8: *Landslides and climatic change*. In *Geomorphological Hazards and Disaster Prevention*, 87.
- Cristea, N. C., J. D. Lundquist, S. P. Loheide, C. S. Lowry, and C. E. Moore (2014), Modelling how vegetation cover affects climate change impacts on streamflow timing and magnitude in the snowmelt-dominated upper Tuolumne Basin, Sierra Nevada, *Hydrological Processes*, doi:10.1002/hyp.9909.
- Cuo, L., T.K. Beyene, N. Voisin, F. Su, D.P. Lettenmaier, M. Alberti, and J.E. Richey. 2011: Effects of mid-twenty-first century climate and land cover change on the hydrology of the Puget Sound basin, Washington. *Hydrological Processes*, 25(11): 1729-1753.
- Curran, C. A., Grossman, E. E., Mastin, M. C., & Huffman, R. L. (2010). Sediment Load and Distribution in the Lower Skagit River. *Skagit County, Washington: US Geological Survey Open-File Report*.
- Czarnowski, M. S., and J. L. Olszewski (1968), Rainfall interception by a forest canopy, *Oikos Supp.*, 19(2),345–350.
- Dai, A. (2008), Temperature and pressure dependence of the rain-snow phase transition over land and ocean, *Geophys. Res. Lett.*, 35, L12802, doi:10.1029/2008GL033295
- Daly, C., W. P. Gibson, G.H. Taylor, G. L. Johnson, P. Pasteris. 2002. A knowledge-based approach to the statistical mapping of climate. *Climate Research*, 22: 99-113
- Daly, C., Halbleib, M., Smith, J.I., Gibson, W.P., Doggett, M.K., Taylor, G.H., Curtis, J., and Pasteris, P.A. 2008. Physiographically-sensitive mapping of temperature and precipitation across the conterminous United States. *International Journal of Climatology*, 28: 2031-2064.
- Di Luzio, M., Johnson, G. L., Daly, C., Eischeid, J. K., & Arnold, J. G. (2008). Constructing retrospective gridded daily precipitation and temperature datasets for the conterminous United States. *Journal of Applied Meteorology and Climatology*, 47(2), 475-497.
- Dulière, V., Zhang, Y., & Salathé Jr, E. P. (2013). Changes in twentieth-century extreme temperature and precipitation over the western United States based on observations and regional climate model simulations\*. *Journal of Climate*, 26(21), 8556-8575. doi:10.1175/JCLI-D-12-00818.1
- Elsner, M. M., Cuo, L., Voisin, N., Deems, J. S., Hamlet, A. F., Vano, J. A., ... & Lettenmaier, D. P. (2010). Implications of 21st century climate change for the hydrology of Washington State. *Climatic Change*, 102(1-2), 225-260.
- Frans, C. 2015. Predicting the role of climate change on glaciated watersheds and the implications for regional water resources sustainability. Ph.D. Dissertation. University of Washington.
- Gao, H., Tang, Q., Shi, X., Zhu, C., Bohn, T. J., Su, F., Sheffield, J., Pan, M., Lettenmaier, D. P., and Wood, E. F. (2010). Water budget record from Variable Infiltration Capacity (VIC) model. *Algorithm Theoretical Basis Document for Terrestrial Water Cycle Data Records*.
- Hamlet, A. F. and D. P. Lettenmaier (2005) *Production of Temporally Consistent Gridded Precipitation and Temperature Fields for the Continental United States* *Journal of Hydrometeorology*, 6, 330-336.
- Hamlet, A.F., M.M. Elsner, G.S. Mauger, S-Y. Lee, I. Tohver, and R.A. Norheim. 2013. An overview of the Columbia Basin Climate Change Scenarios Project: Approach, methods, and summary of key results. *Atmosphere-Ocean* 51(4):392-415, doi: 10.1080/07055900.2013.819555.

- Hegewisch, K.C., Abatzoglou J.T., 2016. An improved Multivariate Adaptive Constructed Analogs (MACA) Statistical Downscaling Method. *In preparation*.
- Henn, B. et al., 2015. Hydroclimatic conditions preceding the March 2014 Oso landslide. *Journal of Hydrometeorology*.
- Homer, C.G., Dewitz, J.A., Yang, L., Jin, S., Danielson, P., Xian, G., Coulston, J., Herold, N.D., Wickham, J.D., and Megown, K., 2015, [Completion of the 2011 National Land Cover Database for the conterminous United States-Representing a decade of land cover change information](#). *Photogrammetric Engineering and Remote Sensing*, v. 81, no. 5, p. 345-354
- Hosking, J. R. M., & Wallis, J. R. (1993). Some statistics useful in regional frequency analysis. *Water Resources Research*, 29(2), 271-281.
- Hosking, J.R.M., 1990. L-moments: analysis and estimation of distributions using linear combinations of order statistics. *Journal of the Royal Statistical Society, Series B*, 52,105-124.
- Hungerford, R.D., Nemani, R.R., Running, S.W., Coughlan, J.C., 1989. MTCLIM: a mountain microclimate simulation model. U.S. Forest Service Intermountain Research Station Research Paper Int-414. Ogden, UT.
- (IPCC) Intergovernmental Panel on Climate Change. 2013. *Working Group 1, Summary for Policymakers*. Available at: [http://www.climatechange2013.org/images/uploads/WGIAR5-SPM\\_Approved27Sep2013.pdf](http://www.climatechange2013.org/images/uploads/WGIAR5-SPM_Approved27Sep2013.pdf)
- Iverson, R. M. et al., 2015. Landslide mobility and hazards: implications of the 2014 Oso disaster, *Earth Planet. Sc. Lett.*, 412, 197–208.
- Kalnay, E., Kanamitsu, M., Kistler, R., Collins, W., Deaven, D., Gandin, L., ... & Zhu, Y. (1996). The NCEP/NCAR 40-year reanalysis project. *Bulletin of the American meteorological Society*, 77(3), 437-471.
- Kelleher, C., T. Wagner, B.L. McGlynn (2015): Model-based analysis of the influence of catchment properties on hydrologic partitioning across five mountain headwater sub-catchments. *Water Resources Research* 51(6):4109-4136. DOI: [10.1002/2014WR016147](https://doi.org/10.1002/2014WR016147)
- Kimball, J.S., Running, S.W., Nemani, R.R., 1997. An improved method for estimating surface humidity from daily minimum temperature. *Agric. For. Meteorol.* 85 (1–2), 87–98, [http://dx.doi.org/10.1016/S0168-1923\(96\)02366-0](http://dx.doi.org/10.1016/S0168-1923(96)02366-0).
- Lee, S. Y., Hamlet, A. F., & Grossman, E. E. (2016). Impacts of Climate Change on Regulated Streamflow, Hydrologic Extremes, Hydropower Production, and Sediment Discharge in the Skagit River Basin. *Northwest Science*, 90(1), 23-43. doi:10.3955/046.090.0104
- Liang, X., Wood, E. F., & Lettenmaier, D. P. (1996). Surface soil moisture parameterization of the VIC-2L model: Evaluation and modification. *Global and Planetary Change*, 13(1), 195-206.
- Liang, X., Lettenmaier, D. P., Wood, E. F., & Burges, S. J. (1994). A simple hydrologically based model of land surface water and energy fluxes for general circulation models. *Journal of Geophysical Research: Atmospheres*, 99(D7), 14415-14428.
- Livneh B., T.J. Bohn, D.S. Pierce, F. Munoz-Ariola, B. Nijssen, R. Vose, D. Cayan, and L.D. Brekke, 2015: A spatially comprehensive, hydrometeorological data set for Mexico, the U.S., and southern Canada 1950-2013, *Nature Scientific Data*, 5:150042, doi:10.1038/sdata.2015.42.
- Livneh B., E.A. Rosenberg, C. Lin, B. Nijssen, V. Mishra, K.M. Andreadis, E.P. Maurer, and D.P. Lettenmaier, 2013: A Long-Term Hydrologically Based Dataset of Land Surface Fluxes and States for the Conterminous United States: Update and Extensions, *Journal of Climate*, 26, 9384–9392.
- Lohmann, D., Raschke, E., Nijssen, B., & Lettenmaier, D. P. (1998). Regional scale hydrology: I. Formulation of the VIC-2L model coupled to a routing model. *Hydrological Sciences Journal*, 43(1), 131-141. doi: 10.1080/02626669809492107
- Lohmann, D., Nolte-Holube, R., & Raschke, E. (1996). A large-scale horizontal routing model to be coupled to land surface parametrization schemes. *Tellus A*, 48(5), 708-721. doi: 10.1034/j.1600-0870.1996.t01-3-00009.x

- Mauger, G.S., J.H. Casola, H.A. Morgan, R.L. Strauch, B. Jones, B. Curry, T.M. Busch Isaksen, L. Whitely Binder, M.B. Krosby, and A.K. Snover, 2015. *State of Knowledge: Climate Change in Puget Sound*. Report prepared for the Puget Sound Partnership and the National Oceanic and Atmospheric Administration. Climate Impacts Group, University of Washington, Seattle. doi:10.7915/CIG93777D
- Maurer, E. P., A. W. Wood, J. C. Adam, D. P. Lettenmaier, and B. Nijssen (2002) *A Long-Term Hydrologically Based Dataset of Land Surface Fluxes and States for the Conterminous United States*, *Journal of Climate*, **15**, 3237-3251.
- Mass, C. et al., 2011. Extreme Precipitation over the West Coast of North America: Is There a Trend?. *Journal of Hydrometeorology*, 12(2), 310-318.
- McKay, L., Bondelid, T., Dewald, T., Johnston, J., Moore, R., and Rea, A., “NHDPlus Version 2: User Guide”, 2012; <https://www.webapps.nwfsc.noaa.gov/wcr/metadata/NHDflowline.htm>
- Meehl, G. A., C. Covey, T. Delworth, M. Latif, B. McAvaney, J. F. B. Mitchell, R. J. Stouffer, and K. E. Taylor, 2007: The WCRP CMIP3 multi-model dataset: A new era in climate change research, *Bulletin of the American Meteorological Society*, **88**, 1383-1394.
- Mendoza, P. A., Clark, M. P., Mizukami, N., Newman, A. J., Barlage, M., Gutmann, E. D., ... & Arnold, J. R. (2015). Effects of hydrologic model choice and calibration on the portrayal of climate change impacts. *Journal of Hydrometeorology*, 16(2), 762-780.
- Minder, J. R., P. W. Mote, and J. D. Lundquist, 2010. [Surface temperature lapse rates over complex terrain: Lessons from the Cascade Mountains](https://doi.org/10.1029/2009JD013493), *J. Geophys. Res.*, 115, D14122, doi:10.1029/2009JD013493.
- Mote, P. W., Rupp, D. E., Abatzoglou, J. T., Hegewisch, K. C., Nijssen, B., Lettenmaier, D. P., Stumbaugh, M., Lee, S.-Y., & Bachelet, D., 2015. Integrated Scenarios for the Future Northwest Environment. Version 2.0. USGS ScienceBase. Data set accessed 2015-03-02 at <https://www.sciencebase.gov/catalog/item/5006eb9de4b0abf7ce733f5c>
- Mote, P. W. et al., 2013. Climate: Variability and Change in the Past and the Future. Chapter 2, 25-40, in M.M. Dalton, P.W. Mote, and A.K. Snover (eds.) *Climate Change in the Northwest: Implications for Our Landscapes, Waters, and Communities*, Washington D.C.: Island Press.
- Nakicenovic, N. et al., 2000. *Special Report on Emissions Scenarios: A Special Report of Working Group III of the Intergovernmental Panel on Climate Change*, Cambridge University Press, Cambridge, U.K., 599 pp. Available online at: <http://www.grida.no/climate/ipcc/emission/index.htm>
- Naz, B. S., Frans, C. D., Clarke, G. K. C., Burns, P., & Lettenmaier, D. P. (2014). Modeling the effect of glacier recession on streamflow response using a coupled glacio-hydrological model. *Hydrology and Earth System Sciences*, 18(2), 787-802.
- Nick, M., Das, S. and Simonovic, S.P. 2011. The Comparison of GEV, Log-Pearson Type 3 and Gumbel Distributions in the Upper Thames River Watershed under Global Climate Models, the University of Western Ontario Department of Civil and Environmental Engineering, Report No:077.
- (NRC) National Research Council. 2012. *Sea-Level Rise for the Coasts of California, Oregon, and Washington: Past, Present, and Future*. Committee on Sea Level Rise in California, Oregon, Washington. Board on Earth Sciences Resources Ocean Studies Board Division on Earth Life Studies The National Academies Press.
- Pacific Climate Impacts Consortium, University of Victoria, and PRISM Climate Group, Oregon State University, (Jan. 2014). High Resolution Climatology. Downloaded from [http://tools.pacificclimate.org/dataportal/bc\\_prism/map/](http://tools.pacificclimate.org/dataportal/bc_prism/map/) on Feb. 16, 2016.
- Rahman, A., Weinmann, P.E. and Mein, R.G. (1999). At-site flood frequency analysis: LP3-product moment, GEV-L moment and GEV-LH moment procedures compared. In: Proceeding Hydrology and Water Resource Symposium, Brisbane, 6–8 July, 2, 715–720.
- Rahman, A., Karin, F. and Rahman, A. 2015. Sampling Variability in Flood Frequency Analysis: How Important is it? 21<sup>st</sup> International Congress on Modelling and Simulation, Gold Coast, Australia, Nov 29-Dec 4, 2015, 2200-2206.

- Rosenberg, E. A. et al., 2010. Precipitation extremes and the impacts of climate change on stormwater infrastructure in Washington State. *Climatic Change*, 102(1-2), 319-349.
- Ruckleshaus Center, December 19<sup>th</sup>, 2012. Chehalis Basin Flood Hazard Mitigation Alternatives Report. *Report to the State of Washington Legislature, Olympia, Washington, USA.*
- Rupp, D. E., Abatzoglou, J. T., Hegewisch, K. C., & Mote, P. W. (2013). Evaluation of CMIP5 20th century climate simulations for the Pacific Northwest USA. *Journal of Geophysical Research: Atmospheres*, 118(19).
- Ryoo, J. M., Y. Kaspi, D. W. Waugh, G. N. Kiladis, D. E. Waliser, E. J. Fetzer, and J. Kim, (2013). Impact of Rossby Wave Breaking on U.S. West Coast Winter Precipitation during ENSO Events. *J. Climate*, 26, 6360-6382.
- Salathé Jr, E. P., Hamlet, A. F., Mass, C. F., Lee, S. Y., Stumbaugh, M., & Steed, R. (2014). Estimates of 21st century flood risk in the Pacific Northwest based on regional climate model simulations. *Journal of Hydrometeorology*, (2014).
- Salathe Jr, E. P., Leung, L. R., Qian, Y., & Zhang, Y. (2010). Regional climate model projections for the State of Washington. *Climatic Change*, 102(1-2), 51-75.
- Scheff, J., & Frierson, D. M. (2012). Robust future precipitation declines in CMIP5 largely reflect the poleward expansion of model subtropical dry zones. *Geophysical Research Letters*, 39(18).
- Skamarock, W. C., Klemp, J. B., Dudhia, J., Gill, D. O., Barker, D. M., Wang, W., & Powers, J. G. (2005). *A description of the advanced research WRF version 2* (No. NCAR/TN-468+ STR). National Center For Atmospheric Research Boulder Co Mesoscale and Microscale Meteorology Div.
- Snover, A.K., Hamlet, A.F., Lettenmaier, D.P. 2003. Climate change scenarios for water planning studies: Pilot applications in the Pacific Northwest. *Bulletin of the American Meteorological Society* 84(11):1513-1518.
- Soil Survey Staff, Natural Resources Conservation Service, United States Department of Agriculture. U.S. General Soil Map (STATSGO2). Available online at <http://sdmdataaccess.nrcs.usda.gov/>.
- Storck, P. (2000), Trees, snow and flooding: An investigation of forest canopy effects on snow accumulation and melt at the plot and watershed scales in the Pacific Northwest, *Water Resour. Ser., Tech. Rep. 161*, Univ. of Wash., Seattle.
- Storck, P., Bowling, L., Wetherbee, P., & Lettenmaier, D. (1998). Application of a GIS-based distributed hydrology model for prediction of forest harvest effects on peak stream flow in the Pacific Northwest. *Hydrological Processes*, 12(6), 889-904.
- Strahler, A. N. (1957). Quantitative analysis of watershed geomorphology. *Eos, Transactions American Geophysical Union*, 38(6), 913-920.
- Sun, N., J. Yearsley, N. Voisin, and D.P. Lettenmaier, 2013: A spatially distributed model for the assessment of land use impacts on stream temperature in small urban watersheds, *Hydrol. Process.* doi: 10.1002/hyp.10363
- Taylor, K. E. et al., 2012. An overview of CMIP5 and the experiment design. *Bulletin of the American Meteorological Society*, 93(4), 485-498, doi:10.1175/BAMS-D-11-00094.1
- Thornton, P.E., Running, S.W., 1999. An improved algorithm for estimating incident daily solar radiation from measurements of temperature, humidity, and precipitation. *Agric. For. Meteorol.* 93 (4), 211–228, [http://dx.doi.org/10.1016/S0168-1923\(98\)00126-9](http://dx.doi.org/10.1016/S0168-1923(98)00126-9).
- Thornton, P.E., Hasenauer, H., White, M.A., 2000. Simultaneous estimation of daily solar radiation and humidity from observed temperature and precipitation: an application over complex terrain in Austria. *Agric. For. Meteorol.* 104 (4), 255–271, [http://dx.doi.org/10.1016/S0168-1923\(00\)00170-2](http://dx.doi.org/10.1016/S0168-1923(00)00170-2).
- Tohver, I. M., Hamlet, A. F., & Lee, S. Y. (2014). Impacts of 21st-Century Climate Change on Hydrologic Extremes in the Pacific Northwest Region of North America. *JAWRA Journal of the American Water Resources Association*, 50(6), 1461-1476.

- Trenberth, K. E. (2011). Changes in precipitation with climate change. *Climate Research*, 47(1-2), 123-138. doi:10.3354/cr00953
- Van Vuuren, D. P. et al., 2011. The representative concentration pathways: An overview. *Climatic Change*, 109(1-2), 5-31.
- Vogel, R.M., McMahon, T.A. and Chiew, F.H.S. (1993). Flood flow frequency model selection in Australia, *Journal Hydrology*, 146, 421-449.
- Wang, Q.J. 1997. LH moments for statistical analysis of extreme events. *Water Resour Res*, 33(12), 2841-2848.
- Warner, M.D., et al. 2015. Changes in Winter Atmospheric Rivers along the North American West Coast in CMIP5 Climate Models. *J. Hydrometeor*, 16, 118–128. doi: <http://dx.doi.org/10.1175/JHM-D-14-0080.1>
- Washington Wildlife Habitat Connectivity Working Group (WHCWG). 2013. An evaluation of the utility of fine-scale, downscaled climate projections for connectivity conservation planning. Washington Departments of Fish and Wildlife, and Transportation, Olympia, WA. <http://waconnected.org/climate-resilient-corridors/>
- Wigmosta, M.S., B. Nijssen, P. Storck, and D.P. Lettenmaier, 2002: The Distributed Hydrology Soil Vegetation Model, In *Mathematical Models of Small Watershed Hydrology and Applications*, V.P. Singh, D.K. Frevert, eds., Water Resource Publications, Littleton, CO., p. 7-42.
- Wigmosta, M. S., Vail, L. W., & Lettenmaier, D. P. (1994). A distributed hydrology-vegetation model for complex terrain. *Water resources research*, 30(6), 1665-1679.

## Appendix A: Links to Project Code, Models, and Data

All results, model files, climate data, and other documentation are linked from main project page (Tables 11, 12). This includes links to the Google map, HTTP archive, and Hydroshare resource (Figure 27). The “Data Structure” section above describes the organization of the streamflow projections.

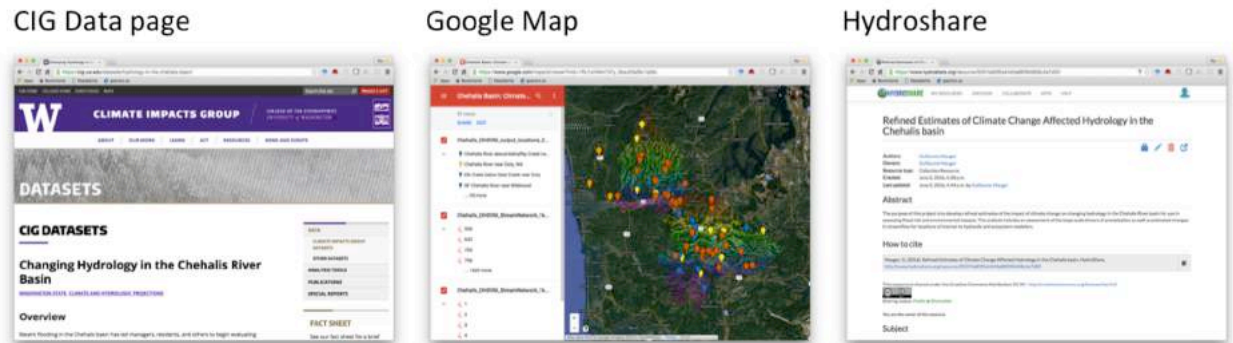


**Figure 27.** Screenshots of the three primarily online resources housing results, source code, and additional details on the project. All resources are linked from the CIG data page (left), including the clickable google map (middle) for viewing streamflow results, and the Hydroshare archive, containing model code, configuration details, and other ancillary information for use in future studies.

**Table 11.** Links to the key project resources, all of which are also linked from the main project page listed in the top row of the table.

<i>Contents</i>	<i>Link</i>
Main project page	<a href="https://cig.uw.edu/datasets/hydrology-in-the-chehalis-basin/">https://cig.uw.edu/datasets/hydrology-in-the-chehalis-basin/</a>
Google Map	<a href="https://www.google.com/maps/d/viewer?mid=1RU1wVMm737y_BbsJ03a1Bc1qh6c">https://www.google.com/maps/d/viewer?mid=1RU1wVMm737y_BbsJ03a1Bc1qh6c</a>
HTTP archive	<a href="http://ces.washington.edu/rocinante/2016_04_ChehalisFlooding/pub/">http://ces.washington.edu/rocinante/2016_04_ChehalisFlooding/pub/</a>
HydroShare resource	<a href="https://www.hydroshare.org/resource/05374e83f5a4443a88f394658c4a7d00/">https://www.hydroshare.org/resource/05374e83f5a4443a88f394658c4a7d00/</a>

**Table 12.** Links to key Hydroshare resources associated with this project. This is a partial listing, intended to illustrate the contents of the resource.

<i>Hydroshare Page</i>	<i>Link</i>
Main Project Page	<a href="https://www.hydroshare.org/resource/05374e83f5a4443a88f394658c4a7d00/">https://www.hydroshare.org/resource/05374e83f5a4443a88f394658c4a7d00/</a>
1/16-degree DEM	<a href="https://www.hydroshare.org/resource/c18cef883695498e81acf9c4260d1e53/">https://www.hydroshare.org/resource/c18cef883695498e81acf9c4260d1e53/</a>
Chehalis DHSVM	<a href="http://www.hydroshare.org/resource/b27a6b3c449e4974bb654eacc8c7f093">http://www.hydroshare.org/resource/b27a6b3c449e4974bb654eacc8c7f093</a>
Chehalis VIC	<a href="http://www.hydroshare.org/resource/f702ce233e7d43fcbef81407ed7327c">http://www.hydroshare.org/resource/f702ce233e7d43fcbef81407ed7327c</a>